

The role of spatial embedding in mouse brain networks constructed from diffusion tractography and tracer injections

Scott Trinkle¹, Sean Foxley¹, Gregg Wildenberg², Narayanan Kasthuri², Patrick La Rivière¹

¹ Department of Radiology, University of Chicago, Chicago, IL, USA

² Department of Neurobiology, University of Chicago, Chicago, IL, USA

Correspondence

Scott Trinkle, Department of Radiology, University of Chicago, 5841 South Maryland Avenue, MC2026, Chicago, IL, 60637
Email: trinkle@uchicago.edu

Abstract

Diffusion MRI tractography is the only noninvasive method to measure the structural connectome in humans. However, recent validation studies have revealed limitations of modern tractography approaches, which lead to significant mistracking caused in part by local uncertainties in fiber orientations that accumulate to produce larger errors for longer streamlines. Characterizing the role of this length bias in tractography is complicated by the true underlying contribution of spatial embedding to brain topology. In this work, we compare graphs constructed with ex vivo tractography data in mice and neural tracer data from the Allen Mouse Brain Connectivity Atlas to random geometric surrogate graphs which preserve the low-order distance effects from each modality in order to quantify the role of geometry in various network properties. We find that geometry plays a substantially larger role in determining the topology of graphs produced by tractography than graphs produced by tracers. Tractography underestimates weights at long distances compared to neural tracers, which leads tractography to place network hubs close to the geometric center of the brain, as do corresponding tractography-derived random geometric surrogates, while tracer graphs place hubs further into peripheral areas of the cortex. We also explore the role of spatial embedding in modular structure, network efficiency and other topological measures in both modalities. Throughout, we compare the use of two different tractography streamline node assignment strategies and find that the overall differences between tractography approaches are small relative to the differences between tractography- and tracer-derived graphs. These analyses help quantify geometric biases inherent to tractography and promote the use of geometric benchmarking in future tractography validation efforts.

Key words: connectome; diffusion MRI; tractography; neural tracer; graph theory; geometric networks

Highlights

- Tractography underestimates long-range connectivity relative to tracers
- Tractography modular and hub-node structure is biased by geometry
- Consideration of geometry is crucial for validation of new tractography approaches.

1 Introduction

The structural connectome¹ is the comprehensive map of connections among all neurons in the brain. Constructing such a map represents a major frontier in neuroscience that relies on the development of novel imaging techniques across a range of spatial scales and model organisms and will provide insight into the basic function and development of the brain² and its pathologies³. Diffusion MRI tractography is currently the only noninvasive method for mapping the human structural connectome⁴ and forms the basis of research initiatives such as the Human Connectome Project⁵. Together with mathematical tools from graph theory^{4,6–8}, tractography studies have helped reveal a number of important network properties in the human brain such as efficiency⁹, modularity¹⁰, and the organization of network hubs¹¹.

Despite these advances, diffusion MRI also suffers from relatively poor spatial resolution and fundamental ambiguities in the mapping between the underlying white matter fiber orientations and the resulting diffusion signal¹². Recent efforts to validate tractography have uncovered several limitations, and even modern approaches still produce high numbers of both false positive and false negative tracts^{13–16}. A specific limitation inherent to probabilistic streamline tractography is the fiber-length bias: local uncertainties in the fiber orientation distribution at each step in the tracking process accumulate to produce global errors for longer streamlines, leading to an underestimation of connectivity weights at greater distances. Characterizing this sort of geometric bias is complicated by the fact that the brain is itself a spatially embedded network with properties partially inherited from geometry: there is a metabolic wiring cost in the establishment of long-range connections, and true falloff of both structural and functional connectivity with distance has been shown with high-resolution invasive imaging as well as tractography in a number of mammalian species^{17–22}. With tractography alone, it is challenging to distinguish the role spatial embedding plays in the true network properties of the brain from the potentially exaggerated representation of that geometric effect resulting from biases inherent to the imaging process.

To characterize methodological biases and improve tractography approaches, tractography experiments need to be validated with additional high-resolution imaging. Optical imaging with neural tracer injections is the gold standard for mesoscale connectivity studies in a number of model organisms^{18,23–27}. Data from the Allen Institute Mouse Brain Connectivity atlas²⁴ form the most comprehensive whole-brain mesoscale brain network in a mammalian species and have been used in previous tractography validation studies, primarily to characterize agreement in voxel-wise streamline density maps with consideration for the role of specific algorithm parameters^{16,28,29}. In this work, we expand the use of the Allen Institute tracer data as a validation tool for tractography connectomics in the mouse brain. Specifically, we use a graph-theoretical approach previously developed for human tractography data²⁰ of benchmarking empirical brain graphs against an ensemble of random geometric surrogates. The random geometric surrogate graphs are constructed from each empirical graph in such a way that the node strength distribution and low-order relationships between connectivity and fiber distance are preserved, but the topology is otherwise destroyed, allowing

for determination of the extent to which certain properties of the mouse structural brain network can be explained through spatial embedding alone.

Previous studies have also explored the influence of spatial embedding and geometry on the topology of the structural brain network in different mammalian species^{17–20,30}. While many of these studies explored the results in an evolutionary context in terms of pressures of wiring cost and efficiency³¹, our aim is instead to use the same tools across the two imaging modalities to specifically assess methodological geometric bias in tractography, taking the tracer-derived network as a significantly higher-fidelity representation of the true mesoscale connectome of the mouse brain. Furthermore, we explore the performance of different tractography approaches by assessing the use of two different streamline node assignment strategies. Accordingly, our analysis aims to do two things: (1) explore and compare the role spatial embedding plays in the topology of graphs derived from tractography and neural tracer imaging and (2) explore the extent to which graphs constructed from different tractography methods reflect the topological properties observed in the empirical tracer model.

2 Methods

2.1 Construction of the primary tracer graph

Our work uses a high-resolution model of the Allen Institute mouse brain structural brain network published by Knox et al.³² The Knox et al. model provides estimates of connectivity at the scale of 100 μm isotropic voxels in the Allen Mouse Brain Common Coordinate Framework (CCF v3), and is derived from 428 whole-brain anterograde fluorescent viral tracer experiments in wild-type C57BL/6J mice collected for the Allen Mouse Brain Connectivity Atlas²⁴. Underlying tracer data are available at <http://connectivity.brain-map.org>. The Knox et al. model can be accessed publicly through the repository available at https://github.com/AllenInstitute/mouse_connectivity_models. While derived from tracer experiments with injection locations that may span multiple distinct regions, the model allows for the efficient creation of regionalized connectivity models using custom brain parcellations based on labeled structures in the Common Coordinate Framework. For this study, we chose to define graph nodes as 286 of the 291 gray matter regions used to construct the regionalized voxel model analyzed in Knox et al³². Five small regions were excluded due to being located almost exactly along the sagittal midline. A full list of gray matter structures used for the parcellation is available in Supporting Information Table S1. The model allows for four different connectivity metrics. Our tracer graph was constructed using the normalized connection density metric, which takes raw projection volume fractions and normalizes them by the volume of the source and target regions for each edge. The anterograde tracers used to produce the Knox et al. model provide a directed graph, whereas tractography graphs are derived from symmetric diffusion data and inherently produce undirected graphs. For fair comparison, the tracer graph was manually made to be undirected by summing

all bidirectional connectivity between every pair of nodes. The Allen Mouse Brain Connectivity Atlas also assumes hemispheric symmetry, as all underlying tracer images were formed from injections into the right hemisphere. Hemispheric symmetry was manually enforced in the final graph in order to yield square connectivity matrices for subsequent analysis.

2.2 Additional tracer data

The Knox et al. model has been shown to outperform the homogeneous model originally published in Oh et al.²⁴ and produces a graph that is nearly 100% fully connected at the scale of the parcellation used in this study. The true density of the whole mouse brain network is an ongoing subject of research. Initial modeling of the Allen Institute data estimated cortical density to vary from 32–52%²⁴ to 59–73%³³. A recent study by Gămănuț, et al.³⁴ observed a much higher cortical density in the mouse brain of 97% using tract-tracing measurements from independent retrograde tracer data. While only available for select ipsilateral intra-cortical edges, the Gămănuț, et al. data have the benefit of representing empirical neuron counts that do not rely on the fixed parcellation template and downstream computational modeling required for the Knox et al. model. Accordingly, our cortical tractography connectivity weights were further benchmarked against these additional weighted connectivity data provided by the authors. These edge-weight values correspond to neuron count fractions within manually defined gray-matter region boundaries corresponding to the parcellation from the Allen Institute (Figure S6B in Gămănuț, et al.³⁴). As with the Knox et al. model, the Gămănuț, et al. cortical subgraph was manually made to be undirected by summing bidirectional connectivity weights between every pair of nodes.

2.3 Animal procedures

Procedures for the collection of the diffusion MRI data used for this study have been published in a previous study³⁵ and are repeated here for completeness. All procedures performed on animals followed protocols approved by the Institutional Animal Care and Use Committee and were in compliance with the Animal Welfare Act and the National Institutes of Health Guide for the Care and Use of Laboratory Animals. Five adult mice were deeply anesthetized with 60 mg/kg pentobarbital and sacrificed by intercardial perfusion with a solution (pH 7.4) of 0.1 M sodium cacodylate and heparin (15 units/ml). This was immediately followed by a solution of 2% paraformaldehyde, 2.5% glutaraldehyde, and 0.1 M sodium cacodylate (pH 7.4). Brains were carefully removed from the skulls and post-fixed in the same fixative overnight at 4°C. Brains were soaked in phosphate buffered saline (PBS) prior to imaging for at least 72 hours to remove fixative from the tissue.

2.4 Diffusion MRI acquisition

Resected mouse brains were dried of excess PBS and placed in 10 ml Falcon tubes. Tubes were filled with Fluorinert (FC-3283, 3M Electronics) for susceptibility matching and to improve shimming. Data were acquired at 9.4 T (20 cm internal diameter, horizontal bore, Bruker BioSpec Small Animal MR System, Bruker Biospin, Billerica, MA) using a 6 cm high performance gradient insert (maximum gradient strength: 1000 mT/m, Bruker Biospin) and a 35 mm internal diameter quadrature volume coil (Rapid MR International, Columbus, Ohio). Third-order shimming was iteratively performed over an ellipse that encompassed the entire brain, but did not extend beyond the boundaries of the Falcon tube/Fluorinert interface, using the Paravision mapshim protocol. Diffusion MRI was performed using a standard diffusion-weighted 3D spin-echo sequence (TR = 600 ms, TE = 11.389 ms, b-value = 3000 s/mm², δ = 3.09 ms, Δ = 6 ms, spatial resolution = 125 μm isotropic, number of b0s = 8, number of directions = 30, receiver bandwidth = 150 kHz, duration = 36h 28min 48s).

2.5 Diffusion MRI processing

Data and diffusion gradient vectors were manually reoriented to the standard RAS neurological display convention. Subsequent processing was performed with the MRtrix3 software package³⁶. Data were denoised using the dwidenoise protocol^{37,38}. Binary brain masks were generated for subsequent processing using the dwi2mask routine. The data were first fit to a diffusion tensor model³⁹ to calculate the fractional anisotropy metric⁴⁰. The data were then fit to fiber orientation distribution functions (fODFs) using constrained spherical deconvolution^{41,42} up to a maximum spherical harmonic order of $\ell_{\max} = 6$ (28 coefficients). The fractional anisotropy image from each dataset was spatially registered to the Allen reference mouse brain template at an isotropic voxel size of 100 μm using affine and diffeomorphic transformations calculated with the ANTS registration package^{43,44}. The Allen template and structure-level annotations in the Common Coordinate Framework were accessed using the allensdk software tool (<https://allensdk.readthedocs.io>). The spatial transforms calculated in ANTS were then applied to the fODFs using the mrtransform protocol in MRTrax3, which applies appropriate reorientation⁴⁵ and modulation⁴⁶ of the fODFs in order to preserve fiber densities across each lobe after transformation.

2.6 Construction of tractography graphs

Probabilistic tractography was performed in MRTrax3 using the iFOD2 algorithm⁴⁷ (step size = 12.5 μm, maximum curvature = 30 μm, minimum length = 0.5 mm, maximum length = 30 mm, fODF cutoff = 0.055). Streamlines were seeded uniformly throughout each of the 286 gray matter regions in the right hemisphere used in the regionalized tracer model, with 2000 seeds per voxel, amounting to around 400 million total streamlines per dataset. Edge weights were determined from each tractography dataset using two different streamline node assignment strategies in order to compare their effects on downstream network structure.

For “endpoint” connectivity, streamlines were assigned to the two nodes corresponding to the gray matter regions closest to their endpoints, within a maximum radius of 125 μm , corresponding to the size of the underlying diffusion data voxels. For “dense” connectivity, streamlines were assigned to all node-pairs corresponding to pairs of gray matter regions they traverse, not just those corresponding to their endpoints. Edge-weight values between two nodes were then taken to be the number of streamlines assigned to the two nodes under both endpoint and dense assignment strategies, resulting in two different graphs per tractography dataset. To match the normalized connection density metric used for the tracer graph, the weights for each node pair were then divided by the product of the two node volumes. As with the tracer graph, hemispheric symmetry was manually enforced to create square connectivity matrices. Also similar to the tracer graph, the probabilistic tractography seeding used in this work led to nearly fully connected graphs.

2.7 Construction of surrogate graphs

The goal for the construction of geometric surrogate graphs was to create an ensemble of graphs that preserve both the distribution of node strengths (the sum of weights at each node) and the low-order weight-distance relationships of a given empirical graph but are otherwise random. Geometric surrogate graphs were constructed from all empirical tracer and tractography graphs by directly following the methodology described in Roberts et al.²⁰, repeated here for completeness. First, the fiber distance between each pair of nodes was quantified based on tractography results. The distance f_{ij} between nodes i and j was defined as the length of the shortest streamline connecting them, averaged across all datasets. To estimate first-order weight-distance effects, we follow Roberts et al. in fitting the logarithm of the edge-weights w_{ij} to a curve given by $\log w_{ij} \approx g(f_{ij})$, where g is a cubic polynomial. This relationship was subtracted from the raw weights, and an additional parabolic curve was then fit to the residuals. After normalizing by this second curve, low-order distance-dependent effects were effectively removed from the weight values and they were randomly shuffled. After randomization, the transformations were applied in reverse order to reimpose low-order weight-distance effects. The original weight values were then reordered to match the random rank order of the surrogate weights. Finally, the node-strength distribution was restored using an iterative procedure that updates the sums of the rows and columns of the surrogate weight matrix towards the empirical values.

This procedure resulted in an ensemble of geometric surrogate graphs W_{geo} for each network construction method that preserve the low-order distance-dependent characteristics and node-strength distribution of the underlying empirical graph W_{emp} , but have all other topological properties destroyed. We make the assumption that network properties that are preserved in the geometric surrogate graphs represent those that have been inherited from the spatial embedding of the brain. Likewise, we assume that differences in network properties between empirical and geometric surrogate graphs represent the extent to which those properties arise from other, non-geometric factors.

A similar procedure without the use of distance transformations was used to construct an ensemble of random surrogate graphs W_{rand} , which preserve the exact strength-sequence of the underlying empirical graphs, but are otherwise completely random. The geometric surrogates W_{geo} represent the null hypothesis that topological properties of brain networks arise from the falloff of edge weights with distance for a given node-strength distribution, while the random surrogates W_{rand} represent the null hypothesis that topological properties of brain networks arise solely from the particular distribution of node strengths and locations.

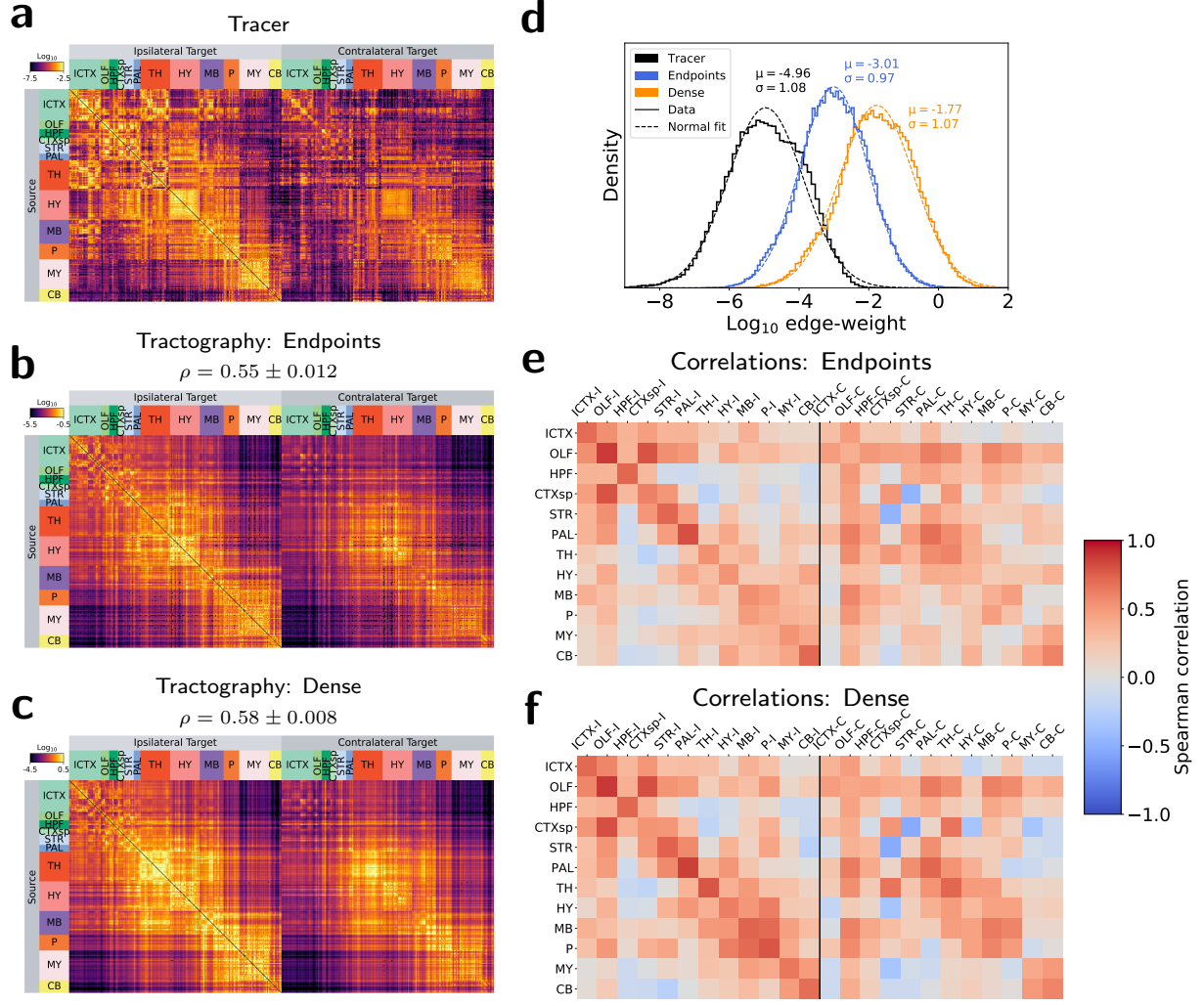


Figure 1: Edge-weight values. (a–c) Connectivity matrices for (a) tracer, (b) endpoint tractography, and (c) dense tractography. Rows represent nodes comprised of 286 gray matter regions across 12 major brain divisions. Columns represent the same nodes for ipsilateral (left) and contralateral (right) connections. Values are shown on a log-color scale spanning five orders of magnitude centered on the mean edge-weight value for each matrix. ρ values represent Spearman rank correlation coefficients between tractography and tracer weights across the whole brain. (d) Edge-weight distributions. Empirical weight histograms (solid lines) with corresponding normal fits (dashed lines). (e–f) Spearman correlations between tracer and (e) endpoint and (f) dense tractography edge-weights across 12 major brain divisions: Isocortex (ICTX), Olfactory areas (OLF), Hippocampal formation (HPF), Cortical subplate (CTXsp), Striatum (STR), Pallidum (PAL), Thalamus (TH), Hypothalamus (HY), Midbrain (MB), Pons (P), Medulla (MY), Cerebellum (CB). “-I” and “-C” in (e–f) refer to ipsilateral and contralateral correlations, respectively. All tractography values represent averages across 5 datasets.

3 Results

Here we report analysis of brain networks constructed using tracer imaging data and two tractography approaches: “endpoints” and “dense” corresponding to two methods of streamline node assignment. For each metric, our goal is to explore how graphs from each tractography approach compare to the tracer graph, specifically with respect to the relationship between empirical and geometric surrogate graphs. Unless otherwise noted, all results labeled “tracer” correspond to the whole-brain graph derived from the Knox et al. connectivity model. All analysis was performed in Python, with graph theoretical measures calculated using the networkx package⁴⁸.

3.1 Comparison of edge-weight values

Structural connectivity matrices and edge-weight distributions are shown for all empirical graphs in Figures 1a–c. Differences in the mean weight values across tractography approaches in Figure 1d follow predictable trends: dense node assignment resulted in higher weights than endpoint node assignment. Note that the physical interpretation of edge weights differs between modalities, so direct comparison of the edge-weight means between modalities is not meaningful. Tracer weights reflect normalized projection volumes and tractography weights reflect normalized streamline counts under different node assignment strategies. Regardless, edge-weight distributions had a comparable and approximately log-normal shape for all empirical graphs.

Overall agreement in edge-weight values was assessed using the Spearman rank correlation coefficient, a nonparametric correlation metric used in previous studies^{28,49} to assess nonlinear agreement between connectivity values. Spearman correlation values between tracer and tractography weights across all edges are shown above each tractography matrix in Figures 1b–c. Edge weights constructed with dense node assignment had a slightly higher Spearman correlation with the tracer weights than those constructed with endpoint node assignment. The difference in correlations was statistically significant ($p < 0.01$) using a t-test. Scatterplots of edge weights between the tracer and tractography graphs are available in Supporting Information Figure S1.

Spearman correlations between tractography and tracer weights assessed at the level of major brain divisions are shown in Figures 1e–f. All tractography methods showed relatively high correlations in ipsilateral intra-division connectivity (diagonals in Figures 1e–f), and weaker contralateral connectivity to homologous regions, reflecting not only a falloff in weight for longer-distance connections, but a falloff in agreement with tracer values. Dense node assignment led to higher Spearman correlations than endpoints for nearly all connections to the pons, and for connections between the hypothalamus, midbrain, and medulla.

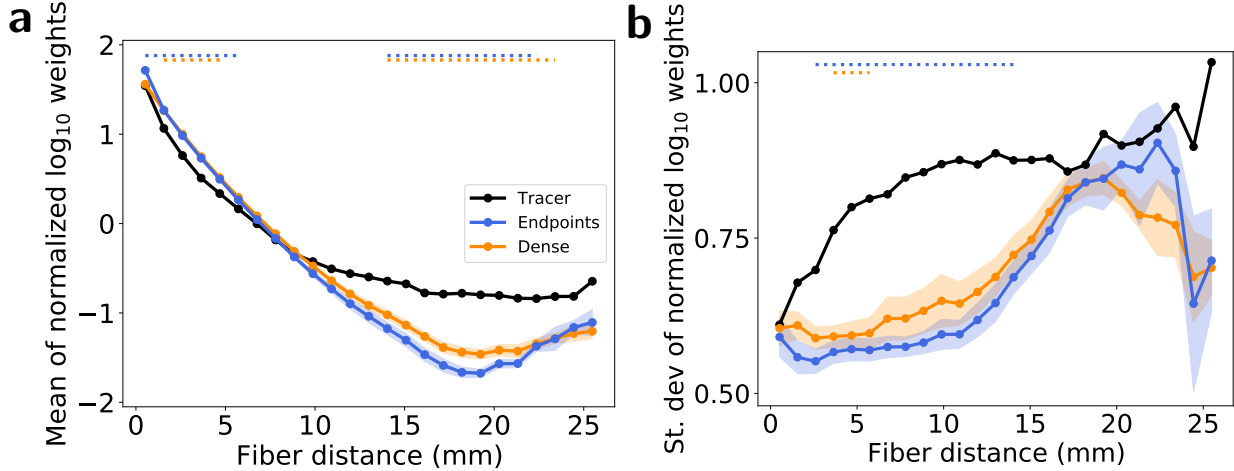


Figure 2: Normalized weight-distance relationships. (a) Circles represent the average log-weight z-scores for each method within 1 mm fiber distance bins. (b) Circles represent the standard deviation of the log-weight z-scores for each method within 1 mm fiber distance bins. Shaded regions represent 1 standard deviation across 5 tractography datasets. The widths of the horizontal lines at the top of each subfigure indicate the range of fiber distance bins with statistically significant differences ($p < 0.01$) between tracer and tractography values for each tractography method, calculated using a one-sample t-test after correcting for multiple comparisons.

3.2 Comparison of weight-distance relationships

The raw weight-distance distributions and polynomial fits used to construct the geometric surrogate graphs are available in Supporting Information Figure S2a–b. Transformed weights (Figure S2c) show effectively zero correlation with fiber distance using both Pearson and Spearman correlation coefficients, indicating that low-order distance relationships have been effectively removed prior to randomization for the construction of the geometric surrogate graphs.

Because the weight values have different physical interpretations for each network construction method, the weight-distance relationships cannot be directly compared. Instead, Figure 2 visualizes the relative relationships between methods after the log-weights were first standardized to zero mean and unit variance. Figure 2a shows the relative falloff of mean normalized log-weights with fiber distance, and Figure 2b shows the change in the standard deviation of normalized log-weights with fiber distance for each method.

The mean normalized weight-distance curves from both tractography graphs in Figure 2a fall below the corresponding tracer curve for distances above around 10 mm, with both tractography methods showing statistically significant differences from tracers for fiber distance between around 17–22 mm. These results suggest that the tractography methods explored in this work underestimate relative long-range connectivity by as much as two orders of magnitude. For most fiber distances, both tractography methods also underestimate the standard deviation of normalized weights compared to tracers. A smaller relative standard deviation around the mean weight-distance relationship is consistent with tractography weights being more

strictly determined by fiber distance than tracer weights are, though these differences were only statistically significant between around 3–15 mm for endpoint node assignment and for a smaller range around 4–6 mm for dense node assignment.

3.3 Comparison of network organization

3.3.1 Modular structure

The modular structure of each brain graph was determined by optimizing the modularity (Q) using the Louvain algorithm⁵⁰. Modularity expresses the extent to which a graph can be subdivided into distinct modules such that intra-modular connectivity is maximized and inter-modular connectivity is minimized⁵¹. The confusion matrices for consensus node-module assignments are shown in Supporting Information Figure S3 for comparisons between empirical tractography and tracer modules as well as between empirical and geometric surrogate modules for all methods. Consensus node-module assignments represent the module ID label most frequently assigned to each node across 5 tractography datasets and ensembles of 100 geometric surrogates. ID labels were first standardized across tractography and geometric surrogate graphs by assigning labels to identified modules such that the overall agreement with the identified modules in the empirical tracer graph was maximized.

The resulting consensus modular decompositions are visualized in physical coordinates for the empirical and geometric surrogate graphs derived with all network construction methods in Figure 3. Spheres represent the physical location of distinct gray-matter nodes, which are colored according to their identified module. Intra-module edges are also visualized as colored lines. Overall, modules identified in the tractography networks are much more spatially clustered together than those in the tracer network. Intra-module edges are more likely to be shorter range for both tractography methods than for tracers, consistent with tractography modular structure being partially determined by geometric bias against long-range connections. This result is further quantified in Table 1, which shows the percent agreement in node-module assignment for pairs of graph construction methods. Graphs from both tractography methods show only modest agreement in module assignment with the tracer graph. The tracer graph also shows only modest agreement in module assignment with its geometric surrogates, suggesting that modules in the true mouse brain network are less spatially clustered than they would be if determined by geometry alone, while both tractography methods show much higher overlap in module assignment between their empirical and geometric surrogates.

Table 1: Percent agreement in consensus node-module assignment.

	Tracer	Endpoints	Dense
Tractography vs. tracer	—	54	54
Empirical vs. geometric surrogates	53	66	67

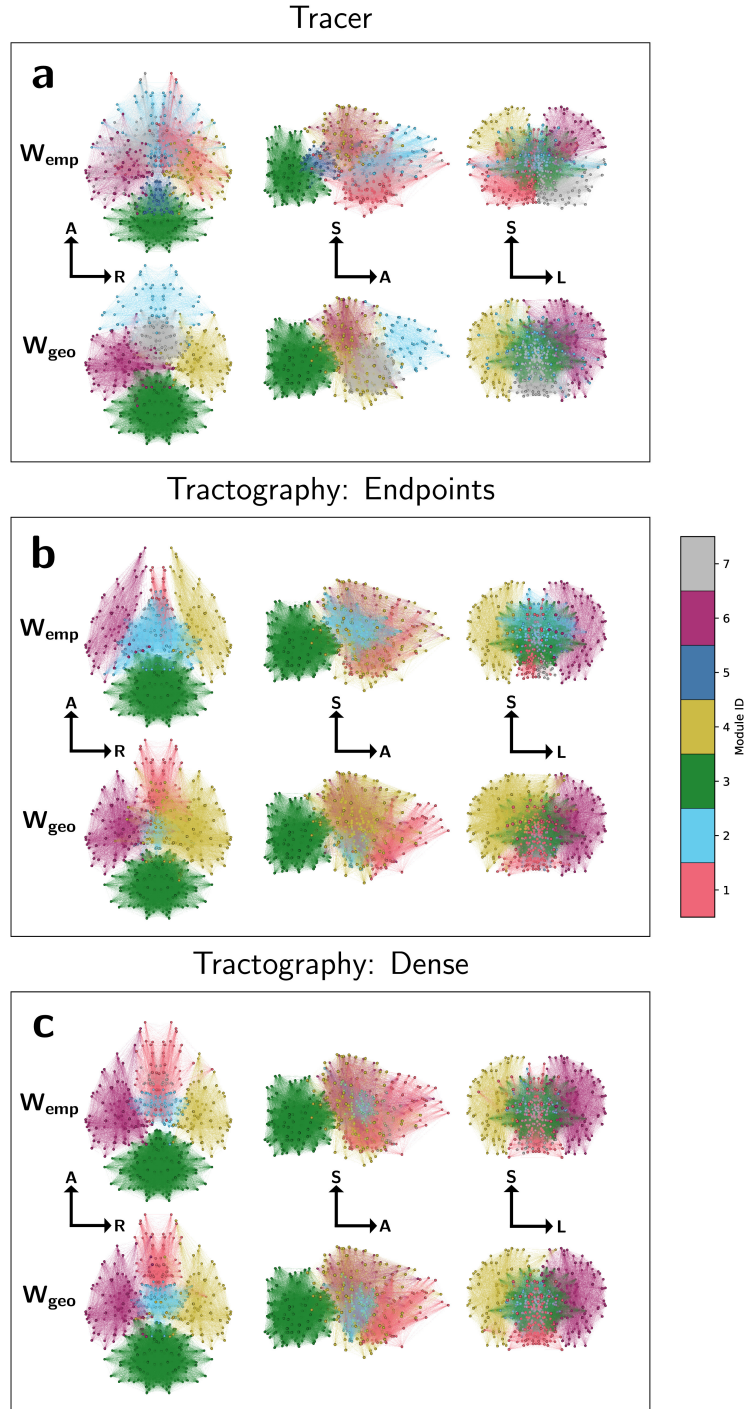


Figure 3: Module diagrams for (a) tracer, (b) endpoint, and (c) dense graphs in physical coordinates. Spheres represent the center of mass of each node, colored by module assignment. Intra-module edges are shown as colored lines. Graphs are visualized along the axial (left), sagittal (middle), and coronal (right) planes with labeled orientations: A=anterior, S=superior, R=right, L=left. Module assignments represent consensus values across 5 empirical tractography graphs and an ensemble of 100 geometric surrogate graphs.

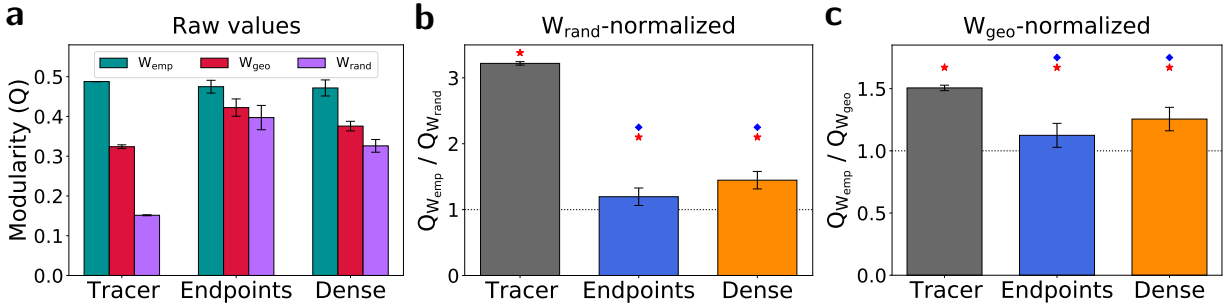


Figure 4: Modularity. (a) Raw Q values for empirical (W_{emp}), geometric surrogate (W_{geo}), and random (W_{rand}) surrogate graphs. Error bars represent 1 standard deviation across 5 tractography datasets for empirical graphs, and 1 standard deviation across ensembles of 100 geometric and random surrogate graphs per method. (b) Empirical Q values normalized by their corresponding mean random surrogate Q value. (c) Empirical Q values normalized by their corresponding mean geometric surrogate Q value. Red stars indicate statistical significance ($p < 0.01$) in the difference between W_{emp} and W_{geo} data calculated with Tukey's range test, and blue diamonds indicate statistical significance ($p < 0.01$) in the difference between W_{rand} - and W_{geo} -normalized tracer and tractography data, calculated with a permutation test.

The optimized Q value itself is a metric of network segregation, indicating a capacity for specialized processing to occur in different regions of the brain. Raw Q values are shown for all graphs in Figure 4a. Figure 4b shows the empirical Q values normalized by the Q values from their corresponding random surrogate graphs, W_{rand} , constructed by randomly shuffling weights within each empirical graph such that the node strength sequence is preserved. While raw Q values are comparable between the tracer and two tractography graphs, the tracer graph shows a substantially higher W_{rand} -normalized modularity relative to all tractography methods, suggesting that tractography graphs under-represent the modularity of the mouse structural brain network beyond what would be expected from a random graph with the same strength sequence. In Figure 4c, empirical Q values have been normalized by the Q values from their corresponding geometric surrogate graphs. This ratio represents the additional modular structure present in the empirical graphs beyond what would be predicted by spatial embedding alone, with a ratio of 1 indicating complete geometric determination. Both tractography methods show values significantly closer to 1 than the tracer graph does. Overall, these results suggest that modular structure in the mouse structural brain network is both underestimated overall and more geometrically determined in tractography relative to neural tracer imaging.

3.3.2 Hub node organization

The arrangement of the subnetwork of central “hub” nodes is key to understanding overall brain network structure. Hub nodes can be identified using a number of complementary centrality measures. The participation coefficient P is based on a particular modular decomposition and expresses the diversity of intermodular connections for a given node, with a value of 1 indicating a node is connected uniformly to

all modules and a value of 0 indicating a node is connected exclusively to its own module^{51,52}. Figure 5 shows scatterplots of participation coefficients for empirical tractography and tracer graphs (Figure 5a–b) and for each empirical graph method and its geometric surrogates (Figure 5c–e). Both tractography methods show only weak correlation with the values from the corresponding tracer graph, but significantly stronger correlations with the values from their own geometric surrogates.

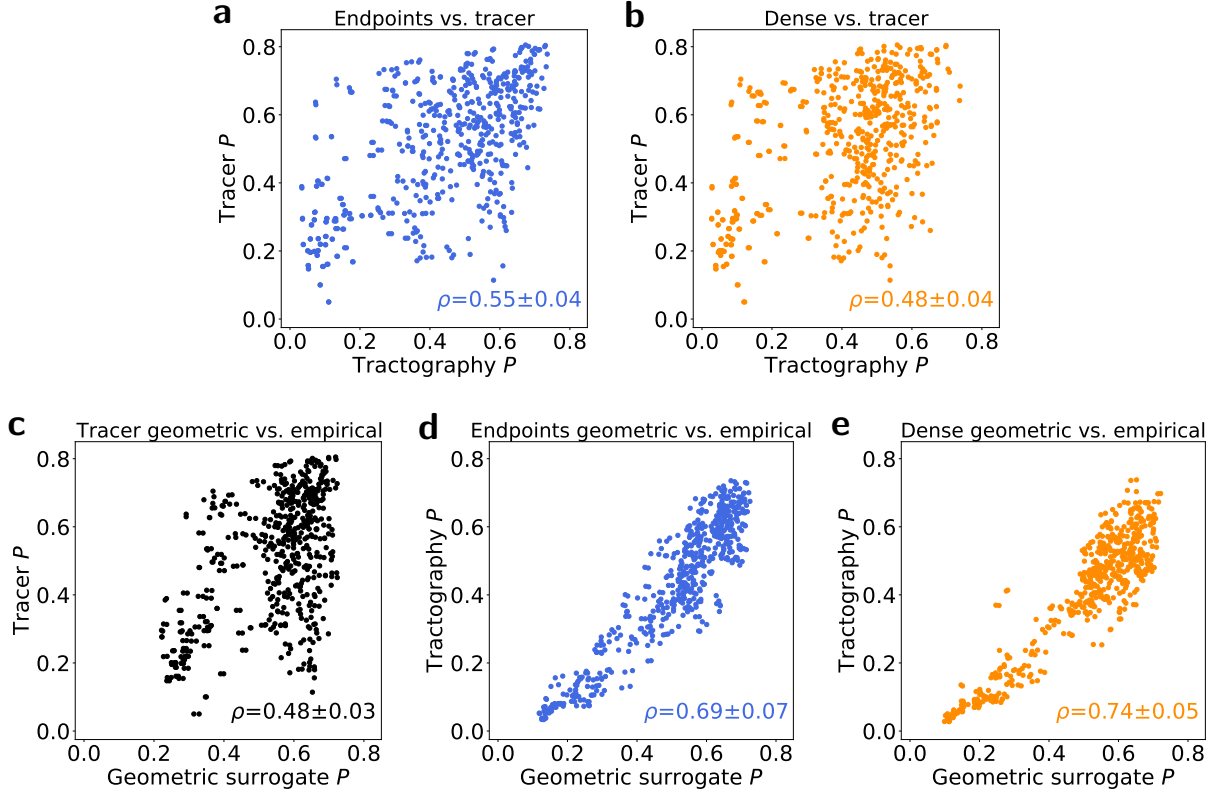


Figure 5: Scatterplots showing the relationship between participation coefficients assigned to each node by different network construction methods. (a–b) Correlations between empirical tracer and empirical (a) endpoints and (b) dense tractography participation coefficients. (c–e) Correlations between empirical (c) tracer, (d) endpoint, and (e) dense participation coefficients and those from their corresponding geometric surrogate graphs. Values represent averages across 5 tractography datasets and an ensemble of 100 geometric surrogate graphs.

Previous work with human tractography datasets²⁰ has revealed that the human brain places its strongest nodes further into geometrically peripheral regions than would be expected by weight-distance effects alone. In Figure 6, we extend this analysis into the mouse brain and compare physical hub organization using node strength as a centrality measure. Hub node locations are visualized in physical coordinates for all empirical and geometric surrogate graphs. Hub nodes are identified as the top 15% of nodes for each graph by node strength and are visualized as large spheres. The remaining bottom 85% of nodes by strength are identified with smaller spheres. Edges between hub nodes are colored teal. For visual clarity, the remaining edges have been omitted.

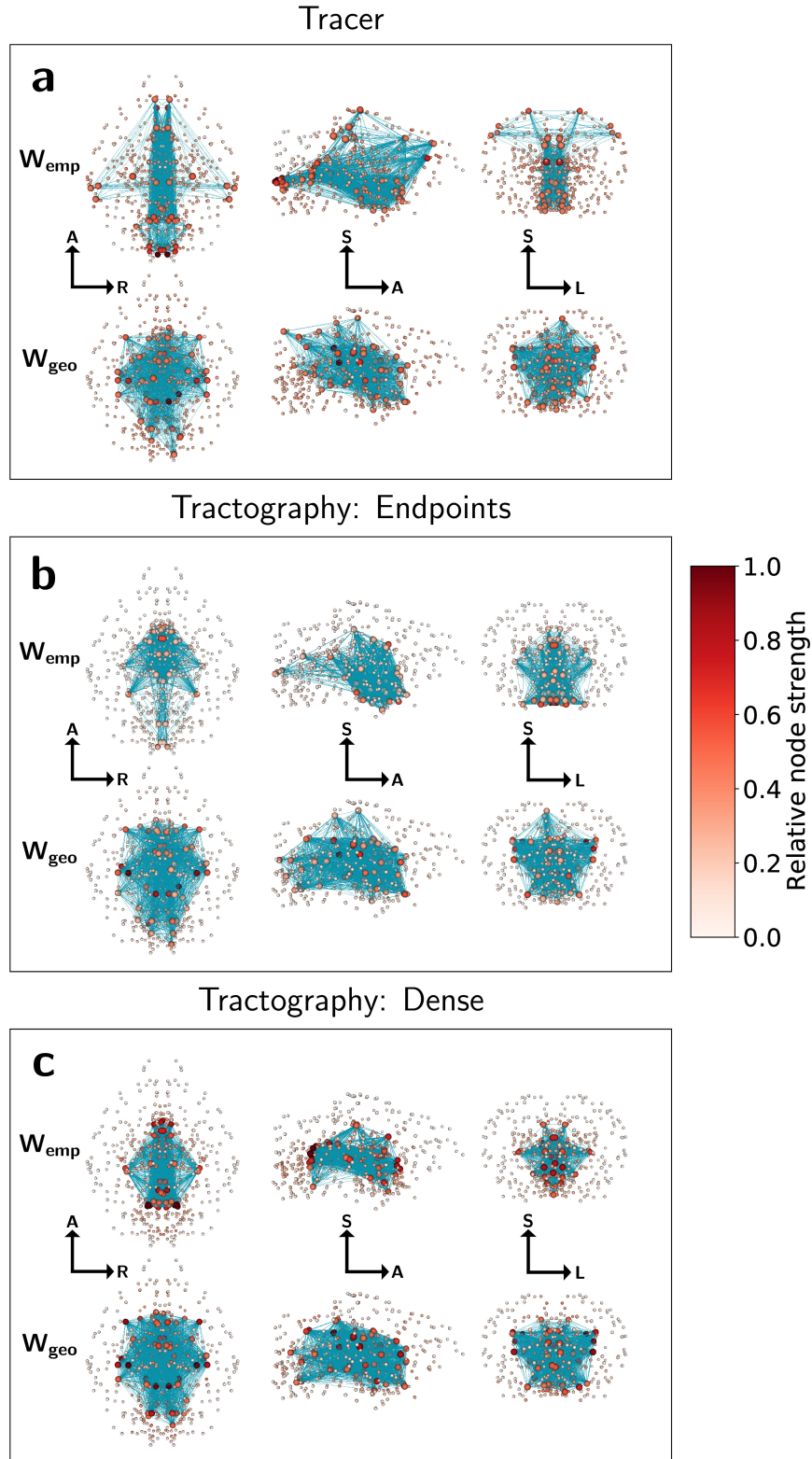


Figure 6: Visualization of network structure for (a) tracer, (b) endpoint, and (c) dense graphs in physical coordinates. Spheres represent the center of mass of each node, colored by relative strength. Edges between the top 15% strongest “hub” nodes (larger spheres) are shown as teal lines. Graphs are visualized along the axial (left), sagittal (middle), and coronal (right) planes with labeled orientations: A=anterior, S=superior, R=right, L=left. Tractography node strengths are calculated as averages across 5 datasets. Geometric surrogate graphs are single representative samples.

Through visual comparison of empirical and geometric surrogate tracer graphs, we find the expected result that the mouse brain network as measured with tracer data places its hub nodes further towards the periphery of the brain than would be predicted by geometry alone, with the strongest nodes located across the isocortex, medulla, and inferior hypothalamus. Empirical tractography graphs, however, place the strongest nodes deeper towards the center of the brain compared to the tracer graph, with hubs organized into a ball-like structure comparable to their corresponding geometric surrogates. Table 2 shows the percent of total hub node strength located within select major brain divisions for each network construction method. 17% of the total tracer hub strength was located along the isocortex, while no isocortex nodes in either of the tractography graphs were identified as hubs. Tractography graphs likewise underestimated hub strength in the medulla and overestimated hub strength in the midbrain and thalamus, particularly for the dense node assignment strategy. Overall, only 11 individual structures were co-identified as hubs between the tracer and both tractography methods.

Table 2: Percent of total hub node strength contained in select major brain divisions.

Region	Tracer	Endpoints	Dense
Hypothalamus	29	57	22
Medulla	19	9	7
Isocortex	17	0	0
Midbrain	10	12	22
Thalamus	9	9	31

In the case of dense node assignment, the tendency to cluster hub nodes near the center of the brain appears even more pronounced than would be predicted by geometric surrogate graphs with the same weight-distance relationship. These results suggest a strong geometric determination in the organization of hub nodes in tractography above and beyond the geometric relationship expected from tracer data.

The geometric centrality of hub nodes is further quantified in Figure 7, which shows the mean distance between hub nodes and the center of mass of the brain for all empirical and geometric surrogate graphs. As visualized in Figure 6, the tracer empirical graph places its hubs further from the center of mass than its corresponding geometric surrogates, while dense tractography not only places its hubs closer to the center of the brain than the tracer graph does, but also places its hubs slightly more central than its own geometric surrogates. Endpoint tractography graphs also place their hub nodes more geometrically central overall than the tracer graph, with distances from the center of mass comparable to their geometric surrogates. However, Figure 6 shows that the endpoint graphs are better able than dense graphs to capture some of the more peripheral hubs along the inferior hypothalamus.

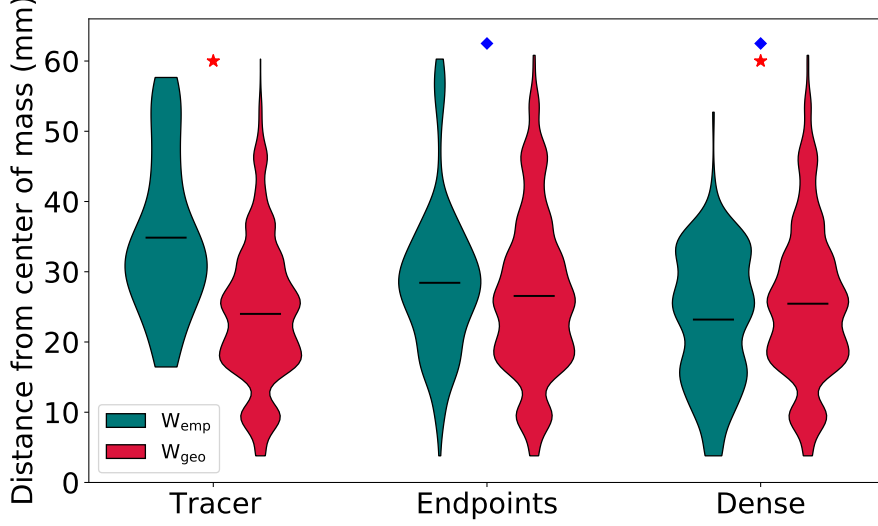


Figure 7: Violin plots showing the distribution of distances between the center of mass of individual hub nodes and the center of mass of the brain. Horizontal bars indicate the means of each distribution. Distributions represent per-node values across all datasets. W_{geo} data are taken from an ensemble of 100 random graphs per network construction method. Red stars indicate statistical significance ($p < 0.01$) in the difference between W_{emp} and W_{geo} data, and blue diamonds indicate statistical significance ($p < 0.01$) in the difference between empirical tracer and tractography data. p -values were calculated using Tukey's range test.

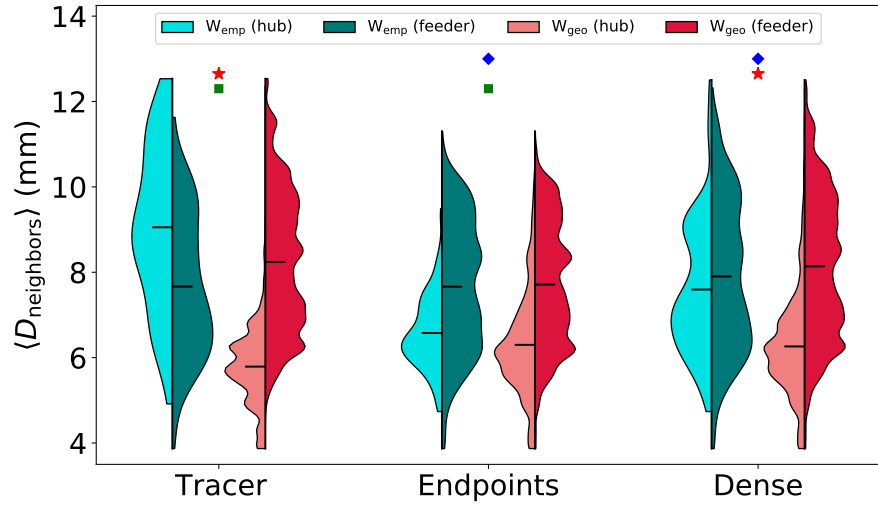


Figure 8: Violin plots showing distributions of the average fiber distance to each node's neighbors, split into hub (top 15%) and feeder (bottom 85%) nodes defined using eigenvector centrality. Distributions from empirical graphs are shown in blue colors, and distributions from geometric surrogate graphs are shown in red colors. Lighter shades of each color indicate hub nodes and darker shades indicate feeder nodes. Horizontal bars indicate the means of each distribution. Distributions represent per-node values across all datasets. Green squares indicate statistical significance ($p < 0.01$) in the difference between empirical hub and feeder distributions. Red stars indicate statistical significance ($p < 0.01$) in the difference between W_{emp} and W_{geo} hub values. Blue diamonds indicate statistical significance ($p < 0.01$) in the difference between empirical tracer and tractography hub values. p -values were calculated using Tukey's range test.

In addition to the participation coefficient and node strength, hubs were identified and characterized using their eigenvector centrality (EC), a robust measure of relative node importance calculated by taking the elements of the leading eigenvector of the connectivity matrix⁵¹. Each node's EC is related to the weight of the connections to its neighbors, such that a node could acquire a high EC either by having a large number of very weak connections or by having a small number of very strong connections.

Figure 8 shows distributions of the average fiber distance to each node's neighbors $\langle D_{\text{neighbors}} \rangle$ for all empirical and geometric surrogate graphs. Distributions are split into hub (top 15%) and “feeder” (bottom 85%) nodes defined using EC. Nodes with a low $\langle D_{\text{neighbors}} \rangle$ imply physical, geometric centrality with respect to their neighbors, and nodes with a high EC imply high topological centrality and node importance.

Geometric surrogate graphs from all network construction methods have much lower mean $\langle D_{\text{neighbors}} \rangle$ for hub nodes than for feeder nodes, meaning they predict the most topologically central hub nodes to also be the most geometrically central. The empirical tracer graph predicts the opposite relationship: not only are tracer hub nodes located further from their neighbors than predicted by geometry, they are also less geometrically central than the remaining feeder nodes, reflecting their peripheral placement seen in Figures 6 and 7.

This effect is not observed in any of the empirical tractography graphs. The dense tractography graphs predict $\langle D_{\text{neighbors}} \rangle$ values for their hub nodes more similar to those from the tracer graph, but the distributions from both tractography approaches are much more similar to those from their corresponding geometric surrogates than the empirical tracer distributions are to theirs. Particularly, both empirical tractography graphs have lower mean $\langle D_{\text{neighbors}} \rangle$ values for hub nodes than for feeder nodes, the reverse of the relationship seen in the tracer graph. This once again indicates a strong geometric bias in the placement of topologically important nodes in tractography graphs.

3.4 Comparison of network efficiency

While analysis of modular structure and related metrics describe aspects of network segregation, the global and local efficiencies are metrics of integration for unweighted networks. Local efficiency is calculated as the average inverse shortest path length between a node and all of its neighbors, while global efficiency is the average inverse shortest path length between all pairs of nodes in a network. Accordingly, networks with high global efficiencies are able to efficiently communicate information across different regions. Raw global efficiency values are shown in Figure 9a. As the underlying weighted graphs are nearly fully connected for all methods, binary efficiencies are characterized as a function of network density after thresholding low-weight edges. Global efficiencies normalized by the values from W_{rand} - and W_{geo} -surrogate graphs are shown in Figures 9b–c, respectively. Across all threshold levels and normalizations, global efficiencies from endpoint tractography provided a good match to those from the tracer model. Dense tractography significantly underestimated global efficiency at all densities, even after normalization with the values from its geometric surrogates, which suggests that dense tractography underestimates the role of geometry

in network integration relative to the tracer model. Figure 9d–e shows scatterplots demonstrating the relationship of per-node local efficiencies between tractography- and tracer-derived networks across multiple densities. Pearson correlations were weak across both methods and all densities, indicating that while endpoint tractography performs well in estimating global efficiency, neither tractography method is able to accurately predict the local efficiency of individual nodes. Plots comparing the additional binary topological properties of clustering coefficient and mean path length are shown in Supporting Information Figures S4–S5.

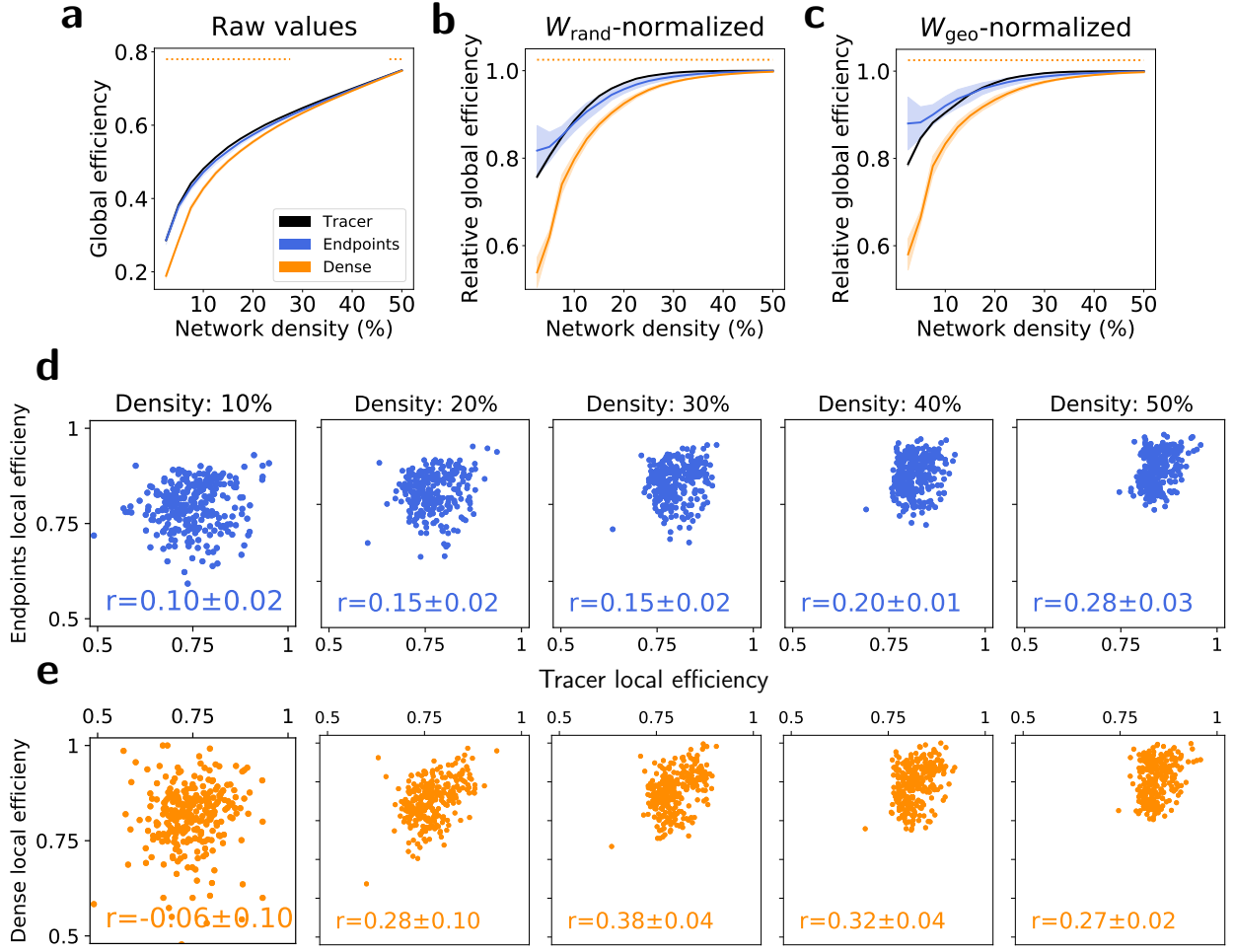


Figure 9: Efficiency. (a–c) Global efficiencies for each method as a function of network density. Shaded regions represent 1 standard deviation across 5 tractography datasets. (a) Raw global efficiency values for all empirical graphs. (b) Global efficiencies for all empirical graphs randomized against the mean value from their corresponding random surrogates. (c) Global efficiencies for all empirical graphs randomized against the mean value from their corresponding geometric surrogates. The widths of the horizontal lines at the top of (a–c) indicate the range of network densities with statistical significance ($p < 0.01$) in the difference between tracer and tractography values for each tractography method, calculated with (a) Tukey's range test and (b–c) a permutation test. (d–e) Scatterplots showing local efficiencies calculated with empirical tracer and (d) endpoint and (e) dense tractography graphs across a range of network densities. r values indicate Pearson correlations.

3.5 Validation with independent tracer measurements

For independent validation of the whole-brain network analysis results from the computational tracer model from Knox et al., tractography edge-weights were also compared to ipsilateral cortical connectivity measurements published in Gămănuț, et al. 2018³⁴. Figures 10a–d show connectivity matrices of 18 cortical regions from both tracer datasets and tractography methods. Scatterplots between tractography and tracer edge-weights are shown for endpoints and dense tractography in Figures 10e–f, respectively. For both node assignment methods, Spearman correlations between tractography and tracer weights are significantly higher with the Knox et al. model than the Gămănuț et al. data. Figure 10g shows the mean relationship between edge weights and fiber distance after the log-weight distributions were normalized to a mean of 0 and standard deviation of 1. Even though the overall range of distances is shorter between ipsilateral cortical nodes than across the whole brain, the tractography methods both still demonstrate a significant underestimation of long-range connectivity relative to empirical tract-tracing measurements in the cortex, which is consistent with the resulting geometric bias in network properties found through comparison to computational tracer-derived connectivity estimates in the whole brain.

4 Discussion

Across nearly all metrics explored in this study, we find that the topological properties of tractography-derived graphs are much more influenced by spatial embedding than would be predicted by the more accurate role of spatial embedding represented by the tracer model. Tractography graphs underestimate connectivity weights at long distances, leading to a conflation of topological and geometric centrality that biases the estimated modular structure and the architecture of hub subnetworks. These results serve as an important reminder for consideration in future tractography studies: given that many properties of the true brain network can be reasonably predicted strictly by spatial embedding, tractography methods development and validation efforts should be targeted towards the ability to predict network properties *beyond* a geometric baseline. While we expect that methodological geometric bias plays a similar role in human tractography networks, some studies have shown encouraging results. For example, Roberts et al.²⁰ demonstrated that empirical human tractography graphs exhibit a more peripheral hub network structure than predicted by their corresponding geometric surrogate graphs, similar to our tracer results in Figure 6 and in contrast to what we observed with tractography networks. Nevertheless, conclusions from human tractography networks cannot be verified with additional ground-truth imaging, and caution should be taken when interpreting tractography-derived brain networks in all species, particularly for metrics which rely more on long-range connections.

One aim of this work was to explore differences in tractography network structure resulting from the streamline node-assignment strategy. Ultimately, we found our results were largely independent of the specific node-assignment approach. The geometric bias in tractography was not mitigated by either method;

despite small differences, network characteristics of both tractography graphs were far more similar to each other than either of them were to characteristics of the tracer graph. While endpoint tractography

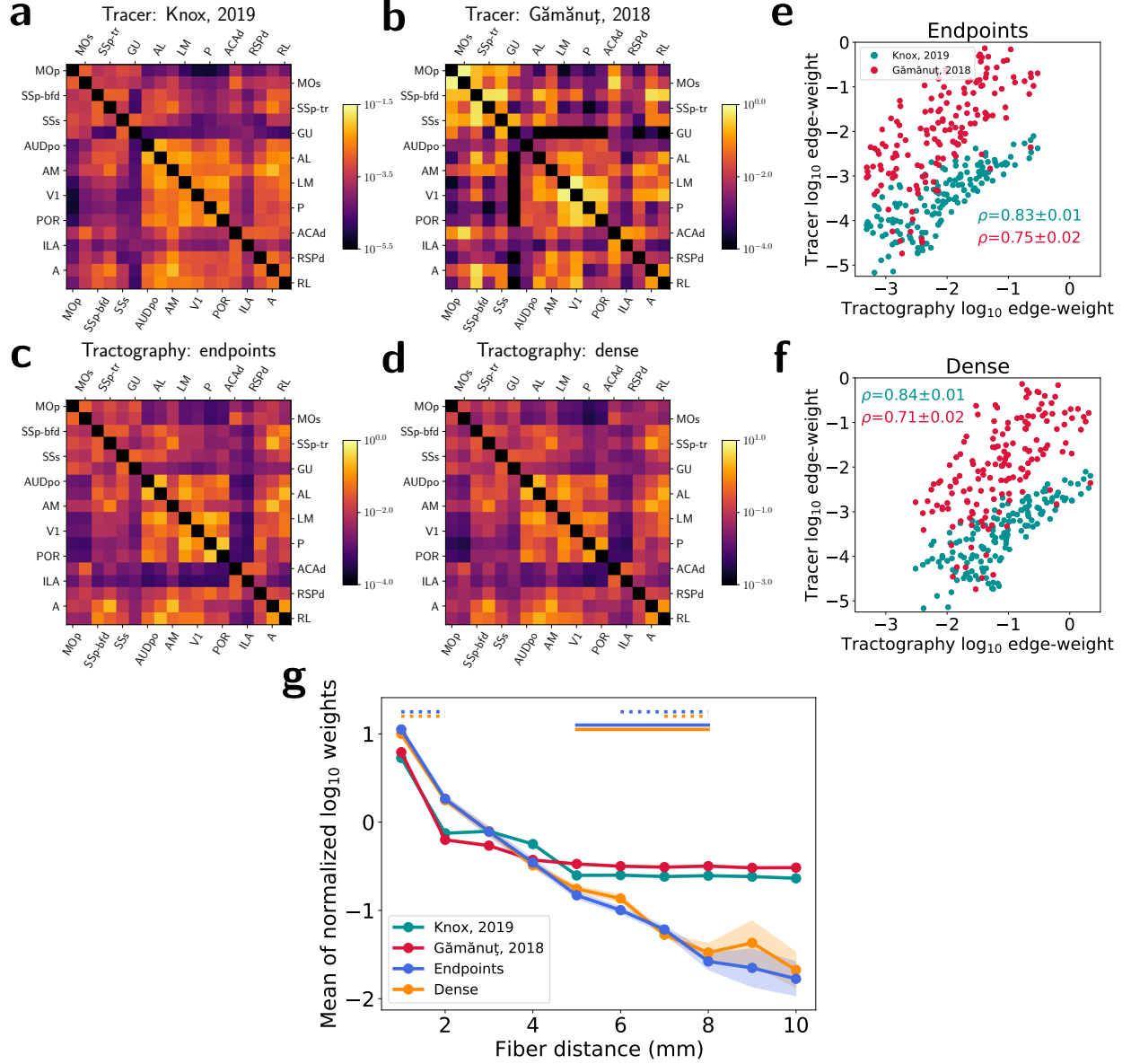


Figure 10: Comparison to empirical, retrograde tracer data in the cortex from Gämänut, 2018. (a-d) Cortical connectivity matrices for (a) the Knox, 2019 tracer model, (b) the Gämänut, 2018 empirical data, (c) endpoint tractography, and (d) dense tractography. (e-f) Scatterplots showing correlations between (e) endpoint and (f) dense tractography edge weights and values from the two tracer graphs. ρ values indicate Spearman correlation coefficients with standard deviations calculated across 5 tractography datasets. (g) Normalized weight-distance relationships. Circles represent the average log-weight z-scores for each method within 1 mm fiber distance bins. Shaded regions represent 1 standard deviation across 5 tractography datasets. The widths of the dotted and solid horizontal lines at the top of the figure indicate the range of fiber distance bins with statistically significant differences ($p < 0.01$) between Knox, 2019 (dotted) and Gämänut, 2018 (solid) tracer values and tractography values for each tractography method, calculated using a one-sample t-test after correcting for multiple comparisons.

might represent a more physically intuitive model of brain connectivity, the comparable performance of dense tractography reflects the ambiguous physical definition of tractography streamlines. Particularly at this spatial resolution and in the absence of stronger anatomical regularization, tractography streamlines strictly represent potential probabilistic pathways of white matter fibers that are consistent with symmetric diffusion data. When streamlines are made to terminate under reasonably enforced constraints such as on fODF magnitude or streamline curvature, this enforces a penalty on unrealistic fiber geometries or the use of lower-confidence diffusion data, but does not yield a physical sense of the actual origin or termination points of the underlying neuronal fibers. This compromises the intuitive appeal of “endpoint” streamline node assignment as used in this study. In fact, without additional constraints, we expect the endpoint locations of any given streamline to be more noisy and erroneous as streamline length increases due to the fiber orientation errors accumulated at each step in the tracking process, an inherent tradeoff that exists even with more sophisticated forms of anatomic regularization. With dense tractography, the effective signal to noise ratio for connectivity similarly falls off for points further away from the seed location, but since a single streamline is allowed to contribute to the connectivity estimate between multiple node-pairs at varying distances, a greater proportion of points from each streamline contribute connectivity estimates that are less noisy than those from the endpoints. Dense tractography also serves as a potentially more physically meaningful match to the tracer data used in this study, as connectivity values in the Knox et al. model are derived from segmented projection volumes of a viral tracer that fluoresces along the entire length of any given neural projection.

The results of this study serve to echo recent tractography validation reviews that suggest that the future of tractography connectomics hinges on the incorporation of more anatomical and microstructural priors to tractography pipelines in order to address geometric and other biases and make streamlines more physically meaningful^{13,15}. A recent study by Girard et al.²⁷ rigorously benchmarked 15 tractography algorithms and a number of regularization approaches such as the “anatomically constrained tractography” framework⁵³ against tracer data in the macaque cortex, though it did not present analysis of downstream network measures. Our future work will similarly explore the adoption of more advanced tractography and regularization approaches in the mouse brain, where whole-brain tracer data are more readily available. Benchmarking these approaches with the use of geometric surrogate graphs will allow for a deeper understanding of the value of existing strategies designed to mitigate tractography biases.

The results in this study rely on the assumption of the tracer data as a ground truth representation of the underlying mesoscale mouse brain network architecture. While histological tracer imaging is certainly ideal in many respects for the benchmarking of diffusion tractography, there are also limitations to this assumption. Both anterograde and retrograde tracer studies produce inherently directed graphs, whereas tractography is based on inherently symmetric diffusion measurements and produces undirected graphs. This requires the use of directional symmetry enforcement for fair comparison that may alter the underlying network properties represented by the tracer data. Besides any biases in the imaging and registration

process itself, the Knox et al. model relies on computational estimates of connectivity based on segmented volume fractions of underlying tracer experiments that may span multiple different gray-matter regions. Accordingly, the Knox et al. model itself is only an estimate that may carry its own biases of the true underlying density of neurons connecting each region pair. For this reason, we are encouraged by the validation of our tractography results against the more empirical measurements of neuronal connectivity from the retrograde tract-tracing experiments published by Gămănuț et al. (Figure 10). Correlations between tractography and tracer edge-weights are even lower for the Gămănuț et al. data than for the Knox et al. model, while tractography shows a comparably dramatic falloff in weight with distance relative to both tracer datasets, suggesting that our overall conclusion that tractography graphs are more determined by geometry than tracer graphs would persist if empirical measurements similar to those from the Gămănuț et al. study were available across the whole brain.

5 Conclusion

We used geometric surrogate graphs to explore the role of spatial embedding in the topological properties of the mouse structural brain network measured by neural tracer imaging and diffusion MRI tractography. We found that spatial embedding played a considerably larger role in the topology of tractography networks than tracer networks. Tractography approaches underestimate long-range connectivity, which leads to geometric biases in the estimated modular structure and placement of high-strength hub nodes. Our results demonstrate the caution required in the interpretation of tractography-derived network measurements that rely on long-range connections and motivate additional geometric consideration in the design of future tractography validation studies.

Acknowledgments and funding

The authors would like to thank Talon Chandler for thoughtful discussions on the role of geometric bias in tractography, as well as Răzvan Gămănuț and Henry Kennedy for their assistance in accessing additional tracer data. This study was funded by the National Institutes of Health (NIH) under grants F31NS113571, R01EB026300, U01MH109100, S10OD025081, S10RR021039, P30CA14599.

Data availability and conflicts of interest

Raw connectivity matrices, distance matrices, and Python code for the construction of geometric and random surrogate graphs are available for download at <http://knowledge.uchicago.edu/record/2846>. The authors declare no conflicts of interest.

References

1. O. Sporns, G. Tononi, and R. Kötter, "The Human Connectome: A Structural Description of the Human Brain", *PLoS Computational Biology*, vol. 1, no. 4, e42, 2005, ISSN: 1553-734X. DOI: [10.1371/journal.pcbi.0010042](https://doi.org/10.1371/journal.pcbi.0010042). [Online]. Available: <https://dx.plos.org/10.1371/journal.pcbi.0010042>.
2. R. E. Passingham, "What we can and cannot tell about the wiring of the human brain", *NeuroImage*, vol. 80, pp. 14–17, Oct. 2013, ISSN: 10538119. DOI: [10.1016/j.neuroimage.2013.01.010](https://doi.org/10.1016/j.neuroimage.2013.01.010). [Online]. Available: <https://linkinghub.elsevier.com/retrieve/pii/S1053811913000414>.
3. A. Griffa, P. S. Baumann, J.-P. Thiran, *et al.*, "Structural connectomics in brain diseases", *NeuroImage*, vol. 80, pp. 515–526, Oct. 2013, ISSN: 10538119. DOI: [10.1016/j.neuroimage.2013.04.056](https://doi.org/10.1016/j.neuroimage.2013.04.056). [Online]. Available: <https://linkinghub.elsevier.com/retrieve/pii/S1053811913004035>.
4. C. Yeh, D. K. Jones, X. Liang, *et al.*, "Mapping Structural Connectivity Using Diffusion <scp>MRI</scp> : Challenges and Opportunities", *Journal of Magnetic Resonance Imaging*, jmri.27188, Jun. 2020, ISSN: 1053-1807. DOI: [10.1002/jmri.27188](https://doi.org/10.1002/jmri.27188). [Online]. Available: <https://onlinelibrary.wiley.com/doi/abs/10.1002/jmri.27188>.
5. M. F. Glasser, S. M. Smith, D. S. Marcus, *et al.*, "The Human Connectome Project's neuroimaging approach", *Nature Neuroscience*, vol. 19, no. 9, pp. 1175–1187, Sep. 2016, ISSN: 1097-6256. DOI: [10.1038/nn.4361](https://doi.org/10.1038/nn.4361). [Online]. Available: <http://www.nature.com/articles/nn.4361>.
6. M. Rubinov and O. Sporns, "Complex network measures of brain connectivity: Uses and interpretations", *NeuroImage*, vol. 52, no. 3, pp. 1059–1069, Sep. 2010, ISSN: 10538119. DOI: [10.1016/j.neuroimage.2009.10.003](https://doi.org/10.1016/j.neuroimage.2009.10.003). [Online]. Available: <https://linkinghub.elsevier.com/retrieve/pii/S105381190901074X>.
7. M. Kaiser, "A tutorial in connectome analysis: Topological and spatial features of brain networks", *NeuroImage*, vol. 57, no. 3, pp. 892–907, Aug. 2011, ISSN: 10538119. DOI: [10.1016/j.neuroimage.2011.05.025](https://doi.org/10.1016/j.neuroimage.2011.05.025). [Online]. Available: <https://linkinghub.elsevier.com/retrieve/pii/S1053811911005131>.
8. A. E. Sizemore, J. Phillips-Cremins, R. Ghrist, *et al.*, "The importance of the whole: topological data analysis for the network neuroscientist", *Network Neuroscience*, vol. 3, no. 3, pp. 656–673, Jun. 2018, ISSN: 24721751. DOI: [10.1162/netn_a_00073](https://doi.org/10.1162/netn_a_00073). arXiv: [1806.05167](https://arxiv.org/abs/1806.05167). [Online]. Available: <http://arxiv.org/abs/1806.05167>.
9. V. Latora and M. Marchiori, "Efficient Behavior of Small-World Networks", *Physical Review Letters*, vol. 87, no. 19, p. 198701, Oct. 2001, ISSN: 0031-9007. DOI: [10.1103/PhysRevLett.87.198701](https://doi.org/10.1103/PhysRevLett.87.198701). arXiv: [0101396](https://arxiv.org/abs/0101396) [cond-mat]. [Online]. Available: <https://link.aps.org/doi/10.1103/PhysRevLett.87.198701>.
10. O. Sporns and R. F. Betzel, "Modular Brain Networks", *Annual Review of Psychology*, vol. 67, no. 1, pp. 613–640, Jan. 2016, ISSN: 0066-4308. DOI: [10.1146/annurev-psych-122414-033634](https://doi.org/10.1146/annurev-psych-122414-033634). [Online]. Available: <http://www.annualreviews.org/doi/10.1146/annurev-psych-122414-033634>.
11. M. P. van den Heuvel and O. Sporns, "Network hubs in the human brain", *Trends in Cognitive Sciences*, vol. 17, no. 12, pp. 683–696, Dec. 2013, ISSN: 13646613. DOI: [10.1016/j.tics.2013.09.012](https://doi.org/10.1016/j.tics.2013.09.012). [Online]. Available: <https://linkinghub.elsevier.com/retrieve/pii/S1364661313002167>.
12. K. Schilling, Y. Gao, V. Janve, *et al.*, "Can increased spatial resolution solve the crossing fiber problem for diffusion MRI?", *NMR in Biomedicine*, vol. 30, no. 12, e3787, Dec. 2017, ISSN: 09523480. DOI: [10.1002/nbm.3787](https://doi.org/10.1002/nbm.3787). [Online]. Available: <http://doi.wiley.com/10.1002/nbm.3787>.
13. K. H. Maier-Hein, P. F. Neher, J.-C. Houde, *et al.*, "The challenge of mapping the human connectome based on diffusion tractography", *Nature Communications*, vol. 8, no. 1, p. 1349, Dec. 2017, ISSN: 2041-1723. DOI: [10.1038/s41467-017-01285-x](https://doi.org/10.1038/s41467-017-01285-x). [Online]. Available: <http://www.nature.com/articles/s41467-017-01285-x>.
14. C. Thomas, F. Q. Ye, M. O. Irfanoglu, *et al.*, "Anatomical accuracy of brain connections derived from diffusion MRI tractography is inherently limited", *Proceedings of the National Academy of Sciences*, vol. 111, no. 46, pp. 16 574–16 579, 2014, ISSN: 0027-8424. DOI: [10.1073/pnas.1405672111](https://doi.org/10.1073/pnas.1405672111). arXiv: [arXiv:1408.1149](https://arxiv.org/abs/1408.1149). [Online]. Available: <http://www.pnas.org/lookup/doi/10.1073/pnas.1405672111>.
15. K. G. Schilling, V. Nath, C. Hansen, *et al.*, "Limits to anatomical accuracy of diffusion tractography using modern approaches", *NeuroImage*, vol. 185, pp. 1–11, Jan. 2019, ISSN: 1053-8119. DOI: [10.1016/J.NEUROIMAGE.2018.10.029](https://doi.org/10.1016/J.NEUROIMAGE.2018.10.029). [Online]. Available: <https://www.sciencedirect.com/science/article/pii/S1053811918319888?via%7B%5C%7D3Dihub>.
16. D. B. Aydogan, R. Jacobs, S. Dulawa, *et al.*, "When tractography meets tracer injections: a systematic study of trends and variation sources of diffusion-based connectivity", *Brain Structure and Function*, vol. 223, no. 6, pp. 2841–2858, Jul. 2018, ISSN: 1863-2653. DOI: [10.1007/s00429-018-1663-8](https://doi.org/10.1007/s00429-018-1663-8). [Online]. Available: <http://link.springer.com/10.1007/s00429-018-1663-8>.
17. S. Horvát, R. Gämänuť, M. Ercsey-Ravasz, *et al.*, "Spatial Embedding and Wiring Cost Constrain the Functional Layout of the Cortical Network of

- Rodents and Primates”, *PLOS Biology*, vol. 14, no. 7, G. Konopka, Ed., e1002512, Jul. 2016, ISSN: 1545-7885. DOI: [10.1371/journal.pbio.1002512](https://doi.org/10.1371/journal.pbio.1002512). [Online]. Available: <https://dx.plos.org/10.1371/journal.pbio.1002512>.
18. M. Ercsey-Ravasz, N. T. Markov, C. Lamy, *et al.*, “A Predictive Network Model of Cerebral Cortical Connectivity Based on a Distance Rule”, *Neuron*, vol. 80, no. 1, pp. 184–197, Oct. 2013, ISSN: 08966273. DOI: [10.1016/j.neuron.2013.07.036](https://doi.org/10.1016/j.neuron.2013.07.036). [Online]. Available: <https://linkinghub.elsevier.com/retrieve/pii/S0896627313006600>.
 19. M. Rubinov, R. J. F. Ypma, C. Watson, *et al.*, “Wiring cost and topological participation of the mouse brain connectome”, *Proceedings of the National Academy of Sciences*, vol. 112, no. 32, pp. 10032–10037, Aug. 2015, ISSN: 0027-8424. DOI: [10.1073/pnas.1420315112](https://doi.org/10.1073/pnas.1420315112). [Online]. Available: <http://www.pnas.org/lookup/doi/10.1073/pnas.1420315112>.
 20. J. A. Roberts, A. Perry, A. R. Lord, *et al.*, “The contribution of geometry to the human connectome”, *NeuroImage*, vol. 124, pp. 379–393, Jan. 2016, ISSN: 10538119. DOI: [10.1016/j.neuroimage.2015.09.009](https://doi.org/10.1016/j.neuroimage.2015.09.009). [Online]. Available: <https://linkinghub.elsevier.com/retrieve/pii/S105381191500806X>.
 21. A. Perinelli, D. Tabarelli, C. Miniussi, *et al.*, “Dependence of connectivity on geometric distance in brain networks”, *Scientific Reports*, vol. 9, no. 1, p. 13412, Dec. 2019, ISSN: 2045-2322. DOI: [10.1038/s41598-019-50106-2](https://doi.org/10.1038/s41598-019-50106-2). [Online]. Available: <http://www.nature.com/articles/s41598-019-50106-2>.
 22. K. Supek, M. Musen, and V. Menon, “Development of Large-Scale Functional Brain Networks in Children”, *PLoS Biology*, vol. 7, no. 7, K. J. Friston, Ed., e1000157, Jul. 2009, ISSN: 1545-7885. DOI: [10.1371/journal.pbio.1000157](https://doi.org/10.1371/journal.pbio.1000157). [Online]. Available: <https://dx.plos.org/10.1371/journal.pbio.1000157>.
 23. S. Jbabdi, S. N. Sotiropoulos, S. N. Haber, *et al.*, “Measuring macroscopic brain connections in vivo”, *Nature Neuroscience*, vol. 18, no. 11, pp. 1546–1555, Nov. 2015, ISSN: 1097-6256. DOI: [10.1038/nn.4134](https://doi.org/10.1038/nn.4134). [Online]. Available: <http://www.nature.com/articles/nn.4134>.
 24. S. W. Oh, J. A. Harris, L. Ng, *et al.*, “A mesoscale connectome of the mouse brain”, *Nature*, vol. 508, no. 7495, pp. 207–214, Apr. 2014, ISSN: 0028-0836. DOI: [10.1038/nature13186](https://doi.org/10.1038/nature13186). [Online]. Available: <http://www.nature.com/articles/nature13186>.
 25. N. T. Markov, M. M. Ercsey-Ravasz, A. R. Ribeiro Gomes, *et al.*, “A Weighted and Directed Interareal Connectivity Matrix for Macaque Cerebral Cortex”, *Cerebral Cortex*, vol. 24, no. 1, pp. 17–36, Sep. 2014, ISSN: 1047-3211. DOI: [10.1093/cercor/bhs270](https://doi.org/10.1093/cercor/bhs270). [Online]. Available: <https://doi.org/10.1093/cercor/bhs270>.
 26. M. Bota, O. Sporns, and L. W. Swanson, “Architecture of the cerebral cortical association connectome underlying cognition”, *Proceedings of the National Academy of Sciences*, vol. 112, no. 16, E2093–E2101, Apr. 2015, ISSN: 0027-8424. DOI: [10.1073/pnas.1504394112](https://doi.org/10.1073/pnas.1504394112). [Online]. Available: <http://www.pnas.org/lookup/doi/10.1073/pnas.1504394112>.
 27. G. Girard, R. Caminiti, A. Battaglia-Mayer, *et al.*, “On the cortical connectivity in the macaque brain: A comparison of diffusion tractography and histological tracing data”, *NeuroImage*, vol. 221, p. 117201, Nov. 2020, ISSN: 10959572. DOI: [10.1016/j.neuroimage.2020.117201](https://doi.org/10.1016/j.neuroimage.2020.117201).
 28. E. Calabrese, A. Badea, G. Cofer, *et al.*, “A Diffusion MRI Tractography Connectome of the Mouse Brain and Comparison with Neuronal Tracer Data”, *Cerebral Cortex*, vol. 25, no. 11, pp. 4628–4637, Nov. 2015, ISSN: 1047-3211. DOI: [10.1093/cercor/bhv121](https://doi.org/10.1093/cercor/bhv121). [Online]. Available: <https://academic.oup.com/cercor/article-lookup/doi/10.1093/cercor/bhv121>.
 29. H. Chen, T. Liu, Y. Zhao, *et al.*, “Optimization of large-scale mouse brain connectome via joint evaluation of DTI and neuron tracing data”, *NeuroImage*, vol. 115, pp. 202–213, Jul. 2015, ISSN: 1053-8119. DOI: [10.1016/j.neuroimage.2015.04.050](https://doi.org/10.1016/j.neuroimage.2015.04.050). [Online]. Available: <https://www.sciencedirect.com/science/article/pii/S105381191500350X?via%205C%20Dihub>.
 30. J. A. Henderson and P. A. Robinson, “Using Geometry to Uncover Relationships Between Isotropy, Homogeneity, and Modularity in Cortical Connectivity”, *Brain Connectivity*, vol. 3, no. 4, pp. 423–437, Aug. 2013, ISSN: 2158-0014. DOI: [10.1089/brain.2013.0151](https://doi.org/10.1089/brain.2013.0151). [Online]. Available: <http://www.liebertpub.com/doi/10.1089/brain.2013.0151>.
 31. E. Bullmore and O. Sporns, “The economy of brain network organization”, *Nature Reviews Neuroscience*, vol. 13, no. 5, pp. 336–349, May 2012, ISSN: 1471-003X. DOI: [10.1038/nrn3214](https://doi.org/10.1038/nrn3214). [Online]. Available: <http://www.nature.com/articles/nrn3214>.
 32. J. E. Knox, K. D. Harris, N. Graddis, *et al.*, “High-resolution data-driven model of the mouse connectome”, *Network Neuroscience*, vol. 3, no. 1, pp. 217–236, Jan. 2019, ISSN: 2472-1751. DOI: [10.1162/netn_a_00066](https://doi.org/10.1162/netn_a_00066). [Online]. Available: https://www.mitpressjournals.org/doi/abs/10.1162/netn%2B5C_%2Da%2B5C_%2D00066.
 33. R. J. F. Ypma and E. T. Bullmore, “Statistical Analysis of Tract-Tracing Experiments Demonstrates a Dense, Complex Cortical Network in the Mouse”, *PLOS Computational Biology*, vol. 12, no. 9, S. Jbabdi, Ed., e1005104, Sep. 2016, ISSN: 1553-7358. DOI: [10.1371/journal.pcbi.1005104](https://doi.org/10.1371/journal.pcbi.1005104). [Online]. Available: <https://dx.plos.org/10.1371/journal.pcbi.1005104>.
 34. R. Gămănuț, H. Kennedy, Z. Toroczkai, *et al.*, “The Mouse Cortical Connectome, Characterized by an Ultra-Dense Cortical Graph, Maintains Specificity by Distinct Connectivity Profiles”, *Neuron*, vol. 97, no. 3,

- 698–715.e10, Feb. 2018, ISSN: 08966273. DOI: [10.1016/j.neuron.2017.12.037](https://doi.org/10.1016/j.neuron.2017.12.037). [Online]. Available: <https://linkinghub.elsevier.com/retrieve/pii/S0896627317311856>.
35. S. Foxley, G. Wildenberg, V. Sampathkumar, *et al.*, “Sensitivity to myelin using model-free analysis of the water resonance line-shape in postmortem mouse brain”, *Magnetic Resonance in Medicine*, mrm.28440, Jul. 2020, ISSN: 0740-3194. DOI: [10.1002/mrm.28440](https://doi.org/10.1002/mrm.28440). [Online]. Available: <https://onlinelibrary.wiley.com/doi/abs/10.1002/mrm.28440>.
36. J.-D. Tournier, R. Smith, D. Raffelt, *et al.*, “MRtrix3: A fast, flexible and open software framework for medical image processing and visualisation”, *NeuroImage*, vol. 202, p. 116 137, Nov. 2019, ISSN: 10538119. DOI: [10.1016/j.neuroimage.2019.116137](https://doi.org/10.1016/j.neuroimage.2019.116137). [Online]. Available: <https://linkinghub.elsevier.com/retrieve/pii/S1053811919307281>.
37. J. Veraart, E. Fieremans, and D. S. Novikov, “Diffusion MRI noise mapping using random matrix theory”, *Magnetic Resonance in Medicine*, vol. 76, no. 5, pp. 1582–1593, Nov. 2016, ISSN: 07403194. DOI: [10.1002/mrm.26059](https://doi.org/10.1002/mrm.26059). [Online]. Available: <http://doi.wiley.com/10.1002/mrm.26059>.
38. J. Veraart, D. S. Novikov, D. Christiaens, *et al.*, “Denoising of diffusion MRI using random matrix theory”, *NeuroImage*, vol. 142, pp. 394–406, Nov. 2016, ISSN: 1053-8119. DOI: [10.1016/j.neuroimage.2016.08.016](https://doi.org/10.1016/j.neuroimage.2016.08.016). [Online]. Available: <https://www.sciencedirect.com/science/article/pii/S1053811916303949?via%7B%5C%7D3Dihub>.
39. P. J. Basser, J. Mattiello, and D. LeBihan, “MR diffusion tensor spectroscopy and imaging.”, *Biophysical journal*, vol. 66, no. 1, pp. 259–67, Jan. 1994, ISSN: 0006-3495. DOI: [10.1016/S0006-3495\(94\)80775-1](https://doi.org/10.1016/S0006-3495(94)80775-1). [Online]. Available: <http://www.ncbi.nlm.nih.gov/pubmed/8130344%20http://www.pubmedcentral.nih.gov/articlerender.fcgi?artid=PMC1275686>.
40. P. J. Basser and C. Pierpaoli, “Microstructural and Physiological Features of Tissues Elucidated by Quantitative-Diffusion-Tensor MRI”, *Journal of Magnetic Resonance, Series B*, vol. 111, no. 3, pp. 209–219, Jun. 1996, ISSN: 1064-1866. DOI: [10.1006/JMRB.1996.0086](https://doi.org/10.1006/JMRB.1996.0086). [Online]. Available: <https://www.sciencedirect.com/science/article/pii/S1064186696900862>.
41. J.-D. Tournier, F. Calamante, D. G. Gadian, *et al.*, “Direct estimation of the fiber orientation density function from diffusion-weighted MRI data using spherical deconvolution”, *NeuroImage*, vol. 23, no. 3, pp. 1176–1185, Nov. 2004, ISSN: 1053-8119. DOI: [10.1016/j.neuroimage.2004.07.037](https://doi.org/10.1016/j.neuroimage.2004.07.037). [Online]. Available: <https://www.sciencedirect.com/science/article/pii/S1053811904004100?via%7B%5C%7D3Dihub>.
42. J.-D. Tournier, F. Calamante, and A. Connelly, “Robust determination of the fibre orientation distribution in diffusion MRI: Non-negativity constrained super-resolved spherical deconvolution”, *NeuroImage*, vol. 35, no. 4, pp. 1459–1472, May 2007, ISSN: 1053-8119. DOI: [10.1016/j.neuroimage.2007.02.016](https://doi.org/10.1016/j.neuroimage.2007.02.016). [Online]. Available: <https://www.sciencedirect.com/science/article/pii/S1053811907001243>.
43. B. B. Avants, C. L. Epstein, M. Grossman, *et al.*, “Symmetric diffeomorphic image registration with cross-correlation: evaluating automated labeling of elderly and neurodegenerative brain”, *Medical image analysis*, vol. 12, no. 1, pp. 26–41, Feb. 2008, ISSN: 1361-8423. DOI: [10.1016/j.media.2007.06.004](https://doi.org/10.1016/j.media.2007.06.004). [Online]. Available: <http://www.ncbi.nlm.nih.gov/pubmed/17659998%20http://www.ncbi.nlm.nih.gov/pmc/articles/PMC2276735/>.
44. A. Klein, J. Andersson, B. A. Ardekani, *et al.*, “Evaluation of 14 nonlinear deformation algorithms applied to human brain MRI registration”, *NeuroImage*, vol. 46, no. 3, pp. 786–802, Jul. 2009, ISSN: 1053-8119. DOI: [10.1016/j.neuroimage.2008.12.037](https://doi.org/10.1016/j.neuroimage.2008.12.037). [Online]. Available: <https://www.sciencedirect.com/science/article/pii/S1053811908012974?via%7B%5C%7D3Dihub>.
45. D. Raffelt, J.-D. Tournier, S. Crozier, *et al.*, “Reorientation of fiber orientation distributions using apodized point spread functions”, *Magnetic Resonance in Medicine*, vol. 67, no. 3, pp. 844–855, Mar. 2012, ISSN: 07403194. DOI: [10.1002/mrm.23058](https://doi.org/10.1002/mrm.23058). [Online]. Available: <http://doi.wiley.com/10.1002/mrm.23058>.
46. D. Raffelt, J.-D. Tournier, S. Rose, *et al.*, “Apparent Fibre Density: A novel measure for the analysis of diffusion-weighted magnetic resonance images”, *NeuroImage*, vol. 59, no. 4, pp. 3976–3994, Feb. 2012, ISSN: 1053-8119. DOI: [10.1016/j.neuroimage.2011.10.045](https://doi.org/10.1016/j.neuroimage.2011.10.045). [Online]. Available: <https://www.sciencedirect.com/science/article/pii/S1053811911012092?via%7B%5C%7D3Dihub>.
47. J.-D. Tournier, F. Calamante, and A. Connelly, “Improved probabilistic streamlines tractography by 2nd order integration over fibre orientation distributions”, in *Proceedings of the International Society for Magnetic Resonance in Medicine*, vol. 1670, 2010. [Online]. Available: <https://cds.isrmr.org/protected/10MProceedings/PDFfiles/1670%7B%5C%7D4298.PDF>.
48. A. A. Hagberg, D. A. Schult, and P. J. Swart, “Exploring network structure, dynamics, and function using NetworkX”, *7th Python in Science Conference (SciPy 2008)*, no. SciPy, pp. 11–15, 2008. [Online]. Available: <http://conference.scipy.org/proceedings/SciPy2008/paper%7B%5C%7D2/>.
49. L. Coletta, M. Pagani, J. D. Whitesell, *et al.*, “Network structure of the mouse brain connectome with

- voxel resolution”, *Science Advances*, vol. 6, no. 51, eabb7187, Dec. 2020, ISSN: 2375-2548. DOI: [10.1126/sciadv.abb7187](https://doi.org/10.1126/sciadv.abb7187). [Online]. Available: <https://advances.sciencemag.org/lookup/doi/10.1126/sciadv.abb7187>.
50. V. D. Blondel, J.-L. Guillaume, R. Lambiotte, *et al.*, “Fast unfolding of communities in large networks”, *Journal of Statistical Mechanics: Theory and Experiment*, vol. 2008, no. 10, P10008, Oct. 2008, ISSN: 1742-5468. DOI: [10.1088/1742-5468/2008/10/P10008](https://doi.org/10.1088/1742-5468/2008/10/P10008). arXiv: 0803.0476. [Online]. Available: <https://iopscience.iop.org/article/10.1088/1742-5468/2008/10/P10008>.
51. M. E. J. Newman, “Analysis of weighted networks”, *Physical Review E - Statistical Physics, Plasmas, Fluids, and Related Interdisciplinary Topics*, vol. 70, no. 5, p. 9, Jul. 2004, ISSN: 1063651X. DOI: [10.1103/PhysRevE.70.056131](https://doi.org/10.1103/PhysRevE.70.056131). arXiv: 0407503 [cond-mat]. [Online]. Available: <http://arxiv.org/abs/cond-mat/0407503%20http://dx.doi.org/10.1103/PhysRevE.70.056131>.
52. R. Guimerà and L. A. Amaral, “Cartography of complex networks: Modules and universal roles”, *Journal of Statistical Mechanics: Theory and Experiment*, no. 2, pp. 1–13, 2005, ISSN: 17425468. DOI: [10.1088/1742-5468/2005/02/P02001](https://doi.org/10.1088/1742-5468/2005/02/P02001).
53. R. E. Smith, J.-D. Tournier, F. Calamante, *et al.*, “Anatomically-constrained tractography: Improved diffusion MRI streamlines tractography through effective use of anatomical information”, *NeuroImage*, vol. 62, no. 3, pp. 1924–1938, Sep. 2012, ISSN: 1053-8119. DOI: [10.1016/j.neuroimage.2012.06.005](https://doi.org/10.1016/j.neuroimage.2012.06.005). [Online]. Available: <https://www.sciencedirect.com/science/article/pii/S1053811912005824?via%7B%5C%7D3Dihub>.

Supporting Information

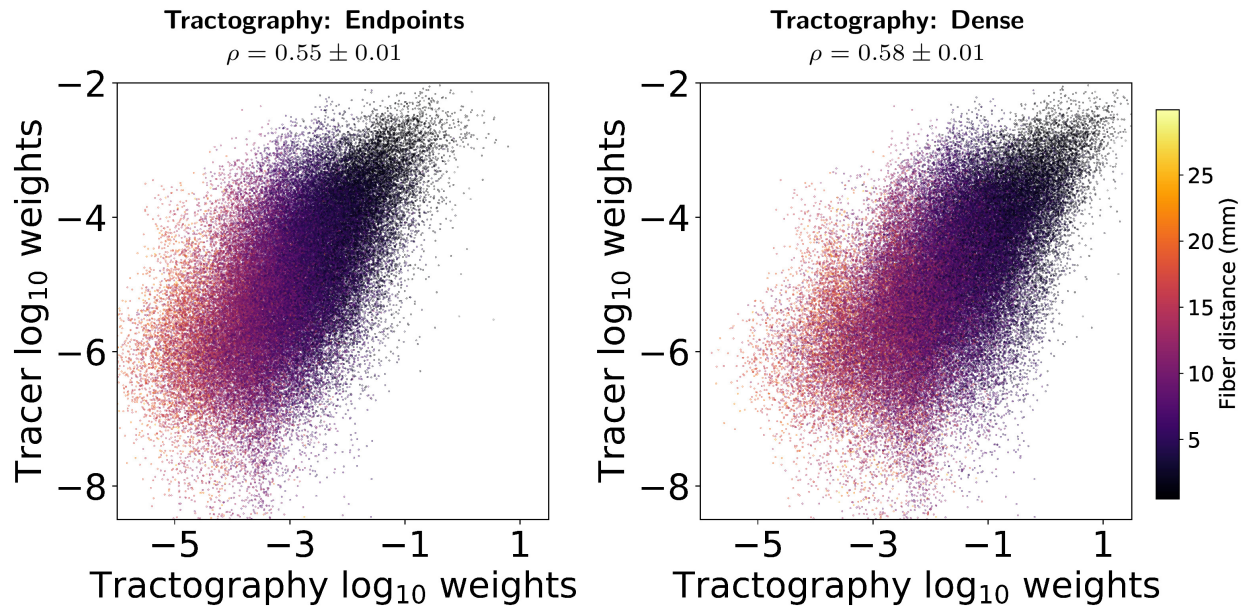


Figure S1: Scatterplots of the log-weights for tracer vs. tractography connectivity matrices. Color indicates fiber distance. Tractography weight values represent averages across 5 datasets. ρ values indicate Spearman rank correlation coefficients, with standard deviations across 5 tractography datasets.

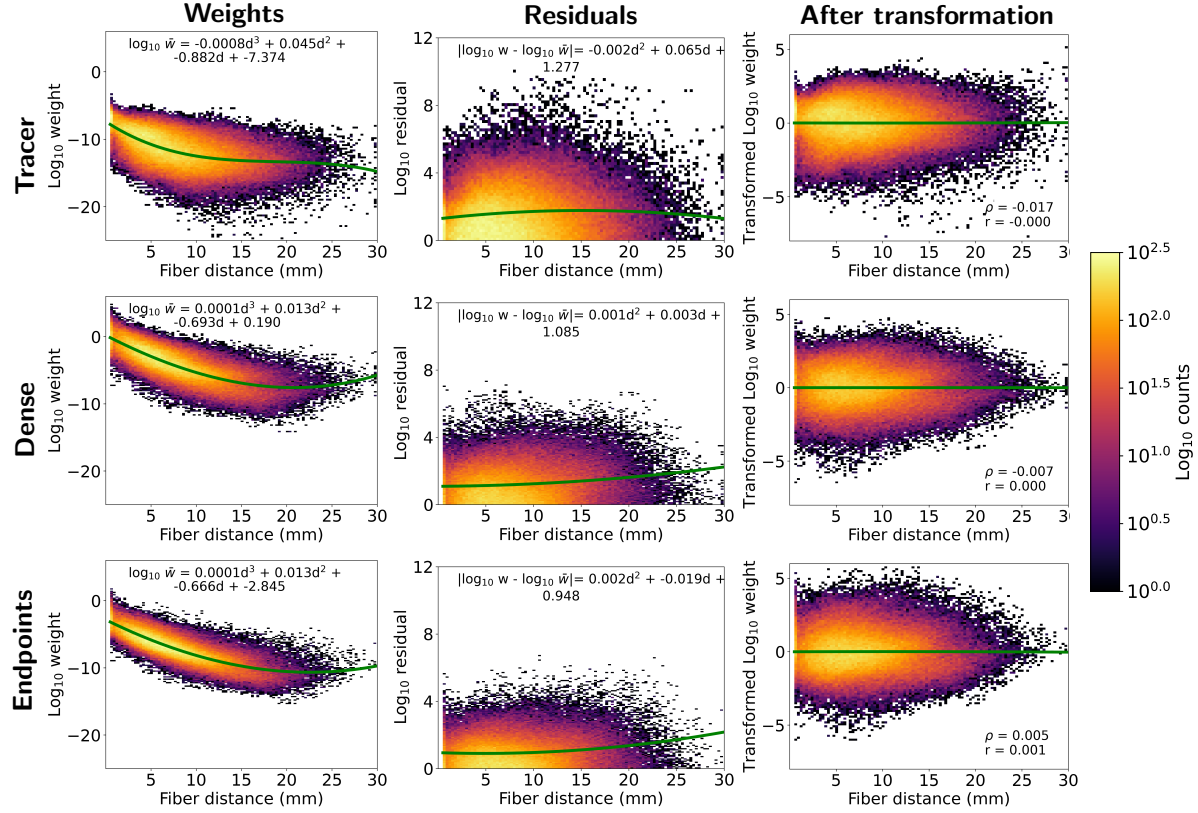


Figure S2: Distance curves for weights (left) and residuals (center) for all network construction methods. The resulting weight-distance relationships after transformation are shown on the right with corresponding linear fits (green line). r and ρ values indicate Pearson and Spearman correlation coefficients, respectively. Counts of individual edges within weight-distance bins are represented as a heatmap on a log color scale. Polynomial fits are shown as green curves. Tractography values represent averages across 5 datasets.

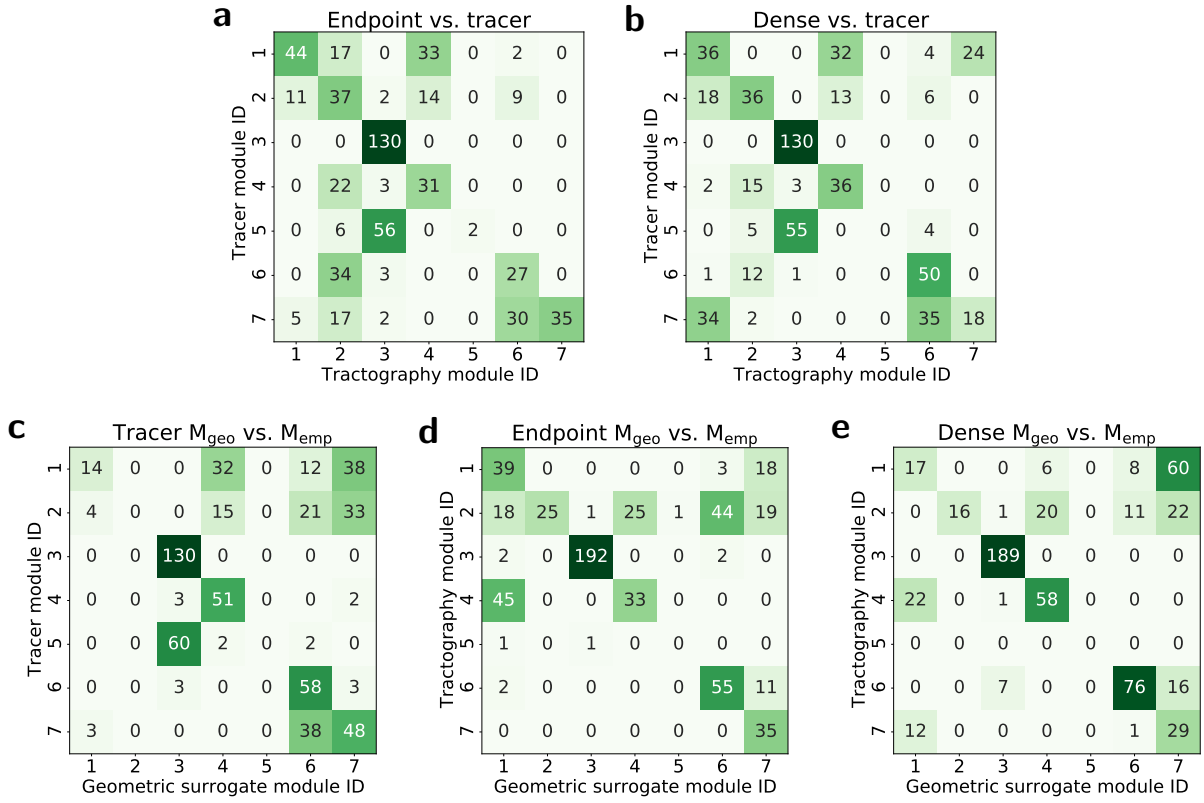


Figure S3: Confusion matrices for module assignment. Module IDs correspond to those identified with the colorbar in Figure 3. (a–b) Module assignments between empirical tracer and empirical (a) endpoints and (b) dense tractography graphs. (c–e) Assignments between empirical (c) tracer, (d) endpoint, and (e) dense graphs and those from their corresponding geometric surrogate graphs. Values represent consensus assignments across 5 tractography datasets and an ensemble of 100 geometric surrogate graphs.

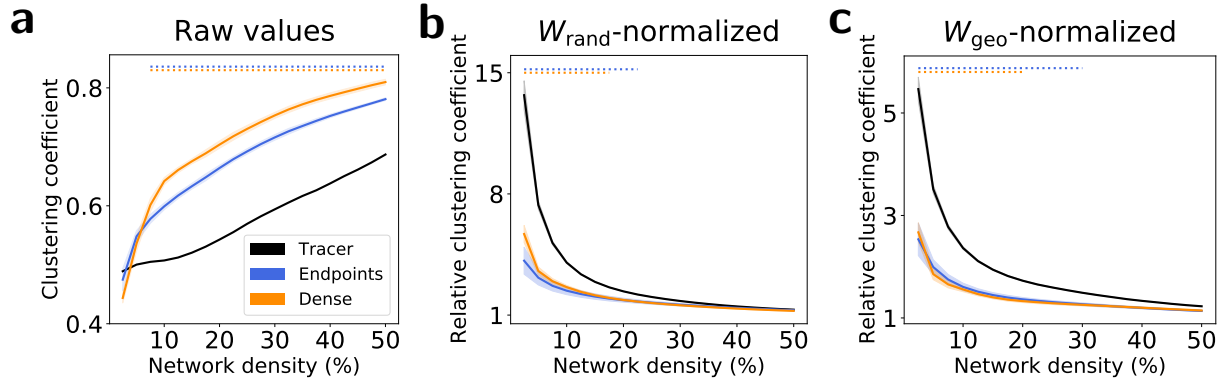


Figure S4: Mean binary clustering coefficients for each method as a function of network density. Shaded regions represent 1 standard deviation across 5 tractography datasets and ensembles of 100 geometric and random surrogate graphs. (a) Raw mean clustering coefficient values for all empirical graphs. (b) Mean clustering coefficients for all empirical graphs randomized against the mean value from their corresponding random surrogates. (c) Mean clustering coefficients for all empirical graphs randomized against the mean value from their corresponding geometric surrogates. The widths of the horizontal lines at the top of the figures indicate the range of network densities with statistical significance ($p < 0.01$) in the difference between tracer and tractography values for each tractography method, calculated with (a) Tukey's range test and (b–c) a permutation test.

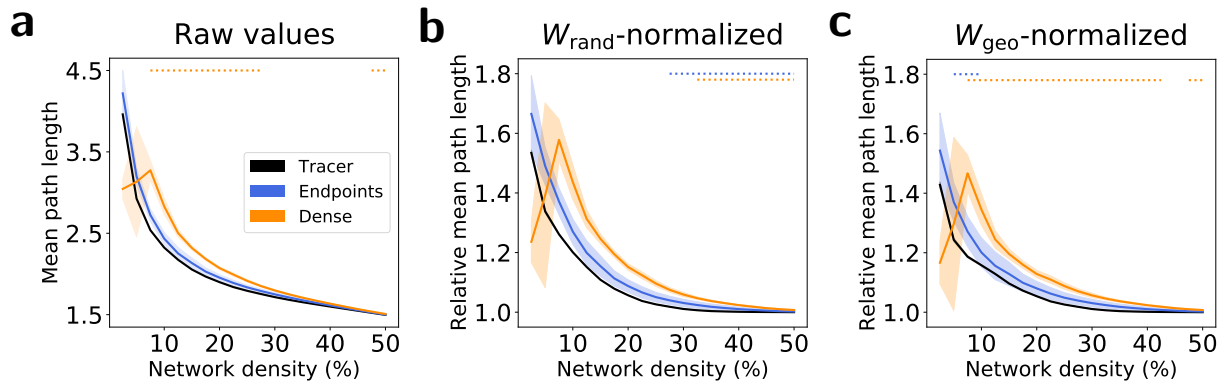


Figure S5: Mean binary path lengths for each method as a function of network density. Shaded regions represent 1 standard deviation across 5 tractography datasets and ensembles of 100 geometric and random surrogate graphs. (a) Raw mean path length values for all empirical graphs. (b) Mean path lengths for all empirical graphs randomized against the mean value from their corresponding random surrogates. (c) Mean path lengths for all empirical graphs randomized against the mean value from their corresponding geometric surrogates. The widths of the horizontal lines at the top of the figures indicate the range of network densities with statistical significance ($p < 0.01$) in the difference between tracer and tractography values for each tractography method, calculated with (a) Tukey's range test and (b–c) a permutation test.

Table S1: Parcellation structure information from the Allen Mouse Brain Atlas.

Abbreviation	Allen structure ID	Full structure name	Major brain division
FRP	184	Frontal pole, cerebral cortex	Isocortex
MOp	985	Primary motor area	Isocortex
MOs	993	Secondary motor area	Isocortex
SSp-n	353	Primary somatosensory area, nose	Isocortex
SSp-bfd	329	Primary somatosensory area, barrel field	Isocortex
SSp-II	337	Primary somatosensory area, lower limb	Isocortex
SSp-m	345	Primary somatosensory area, mouth	Isocortex
SSp-ul	369	Primary somatosensory area, upper limb	Isocortex
SSp-tr	361	Primary somatosensory area, trunk	Isocortex
SSp-un	182305689	Primary somatosensory area, unassigned	Isocortex
SSs	378	Supplemental somatosensory area	Isocortex
GU	1057	Gustatory areas	Isocortex
VISC	677	Visceral area	Isocortex
AUDd	1011	Dorsal auditory area	Isocortex
AUDp	1002	Primary auditory area	Isocortex
AUDpo	1027	Posterior auditory area	Isocortex
AUDv	1018	Ventral auditory area	Isocortex
VISal	402	Anterolateral visual area	Isocortex
VISam	394	Anteromedial visual area	Isocortex
VISI	409	Lateral visual area	Isocortex
VISp	385	Primary visual area	Isocortex
VISpl	425	Posterolateral visual area	Isocortex
VISpm	533	posteromedial visual area	Isocortex
VISli	312782574	Laterointermediate area	Isocortex
VISpor	312782628	Postrhinal area	Isocortex
ACAd	39	Anterior cingulate area, dorsal part	Isocortex
ACAv	48	Anterior cingulate area, ventral part	Isocortex
PL	972	Prelimbic area	Isocortex
ILA	44	Infralimbic area	Isocortex
ORBI	723	Orbital area, lateral part	Isocortex
ORBm	731	Orbital area, medial part	Isocortex
ORBvl	746	Orbital area, ventrolateral part	Isocortex
Ald	104	Agranular insular area, dorsal part	Isocortex
Alp	111	Agranular insular area, posterior part	Isocortex
Alv	119	Agranular insular area, ventral part	Isocortex
RSPagl	894	Retrosplenial area, lateral agranular part	Isocortex
RSPd	879	Retrosplenial area, dorsal part	Isocortex
RSPv	886	Retrosplenial area, ventral part	Isocortex
VISa	312782546	Anterior area	Isocortex
VISrl	417	Rostrolateral visual area	Isocortex
TEa	541	Temporal association areas	Isocortex
PERI	922	Perirhinal area	Isocortex
ECT	895	Ectorhinal area	Isocortex
MOB	507	Main olfactory bulb	Olfactory areas
AOB	151	Accessory olfactory bulb	Olfactory areas
AON	159	Anterior olfactory nucleus	Olfactory areas
TT	589	Taenia tecta	Olfactory areas
DP	814	Dorsal peduncular area	Olfactory areas
PIR	961	Piriform area	Olfactory areas
NLOT	619	Nucleus of the lateral olfactory tract	Olfactory areas
COAa	639	Cortical amygdalar area, anterior part	Olfactory areas
COAp	647	Cortical amygdalar area, posterior part	Olfactory areas
PAA	788	Piriform-amygdalar area	Olfactory areas
TR	566	Postpiriform transition area	Olfactory areas
CA1	382	Field CA1	Hippocampal formation
CA2	423	Field CA2	Hippocampal formation
CA3	463	Field CA3	Hippocampal formation
DG	726	Dentate gyrus	Hippocampal formation
FC	982	Fasciola cinerea	Hippocampal formation
IG	19	Induseum griseum	Hippocampal formation
ENTI	918	Entorhinal area, lateral part	Hippocampal formation
ENTm	926	Entorhinal area, medial part, dorsal zone	Hippocampal formation
PAR	843	Parasubiculum	Hippocampal formation
POST	1037	Postsubiculum	Hippocampal formation

Continued on next page

Continued from previous page

Abbreviation	Allen structure ID	Full structure name	Major brain division
PRE	1084	Presubiculum	Hippocampal formation
SUB	502	Subiculum	Hippocampal formation
CLA	583	Clastrum	Cortical subplate
EPd	952	Endopiriform nucleus, dorsal part	Cortical subplate
EPv	966	Endopiriform nucleus, ventral part	Cortical subplate
LA	131	Lateral amygdalar nucleus	Cortical subplate
BLA	295	Basolateral amygdalar nucleus	Cortical subplate
BMA	319	Basomedial amygdalar nucleus	Cortical subplate
PA	780	Posterior amygdalar nucleus	Cortical subplate
CP	672	Caudoputamen	Striatum
ACB	56	Nucleus accumbens	Striatum
FS	998	Fundus of striatum	Striatum
OT	754	Olfactory tubercle	Striatum
LSc	250	Lateral septal nucleus, caudal (caudodorsal) part	Striatum
LSr	258	Lateral septal nucleus, rostral (rostroventral) part	Striatum
LSv	266	Lateral septal nucleus, ventral part	Striatum
SF	310	Septofimbrial nucleus	Striatum
SH	333	Septohippocampal nucleus	Striatum
AAA	23	Anterior amygdalar area	Striatum
BA	292	Bed nucleus of the accessory olfactory tract	Striatum
CEA	536	Central amygdalar nucleus	Striatum
IA	1105	Intercalated amygdalar nucleus	Striatum
MEA	403	Medial amygdalar nucleus	Striatum
GPe	1022	Globus pallidus, external segment	Pallidum
GPi	1031	Globus pallidus, internal segment	Pallidum
SI	342	Substantia innominata	Pallidum
MA	298	Magnocellular nucleus	Pallidum
MS	564	Medial septal nucleus	Pallidum
NDB	596	Diagonal band nucleus	Pallidum
TRS	581	Triangular nucleus of septum	Pallidum
BST	351	Bed nuclei of the stria terminalis	Pallidum
BAC	287	Bed nucleus of the anterior commissure	Pallidum
VAL	629	Ventral anterior-lateral complex of the thalamus	Thalamus
VM	685	Ventral medial nucleus of the thalamus	Thalamus
VPL	718	Ventral posterolateral nucleus of the thalamus	Thalamus
VPLpc	725	Ventral posterolateral nucleus of the thalamus, parvicellular part	Thalamus
VPM	733	Ventral posteromedial nucleus of the thalamus	Thalamus
VPMpc	741	Ventral posteromedial nucleus of the thalamus, parvicellular part	Thalamus
SPFm	414	Subparafascicular nucleus, magnocellular part	Thalamus
SPFp	422	Subparafascicular nucleus, parvicellular part	Thalamus
SPA	609	Subparafascicular area	Thalamus
PP	1044	Peripeduncular nucleus	Thalamus
MG	475	Medial geniculate complex	Thalamus
LGd	170	Dorsal part of the lateral geniculate complex	Thalamus
LP	218	Lateral posterior nucleus of the thalamus	Thalamus
PO	1020	Posterior complex of the thalamus	Thalamus
POL	1029	Posterior limiting nucleus of the thalamus	Thalamus
SGN	325	Suprageniculate nucleus	Thalamus
AV	255	Anteroventral nucleus of thalamus	Thalamus
AM	127	Anteromedial nucleus	Thalamus
AD	64	Anterodorsal nucleus	Thalamus
IAM	1120	Interanteromedial nucleus of the thalamus	Thalamus
IAD	1113	Interanterodorsal nucleus of the thalamus	Thalamus
LD	155	Lateral dorsal nucleus of thalamus	Thalamus
IMD	59	Intermediodorsal nucleus of the thalamus	Thalamus
MD	362	Mediodorsal nucleus of thalamus	Thalamus
SMT	366	Submedial nucleus of the thalamus	Thalamus
PR	1077	Perireunenesis nucleus	Thalamus
PVT	149	Paraventricular nucleus of the thalamus	Thalamus
PT	15	Parataenial nucleus	Thalamus
RE	181	Nucleus of reunions	Thalamus
RH	189	Rhomboid nucleus	Thalamus
CM	599	Central medial nucleus of the thalamus	Thalamus
PCN	907	Paracentral nucleus	Thalamus
CL	575	Central lateral nucleus of the thalamus	Thalamus

Continued on next page

Continued from previous page

Abbreviation	Allen structure ID	Full structure name	Major brain division
PF	930	Parafascicular nucleus	Thalamus
RT	262	Reticular nucleus of the thalamus	Thalamus
IGL	27	Intergeniculate leaflet of the lateral geniculate complex	Thalamus
LGv	178	Ventral part of the lateral geniculate complex	Thalamus
SubG	321	Subgeniculate nucleus	Thalamus
MH	483	Medial habenula	Thalamus
LH	186	Lateral habenula	Thalamus
SO	390	Supraoptic nucleus	Hypothalamus
ASO	332	Accessory supraoptic group	Hypothalamus
PVH	38	Paraventricular hypothalamic nucleus	Hypothalamus
PVa	30	Periventricular hypothalamic nucleus, anterior part	Hypothalamus
PVi	118	Periventricular hypothalamic nucleus, intermediate part	Hypothalamus
ARH	223	Arcuate hypothalamic nucleus	Hypothalamus
ADP	72	Anterodorsal preoptic nucleus	Hypothalamus
AVP	263	Anteroventral preoptic nucleus	Hypothalamus
AVPV	272	Anteroventral periventricular nucleus	Hypothalamus
DMH	830	Dorsomedial nucleus of the hypothalamus	Hypothalamus
MEPO	452	Median preoptic nucleus	Hypothalamus
MPO	523	Medial preoptic area	Hypothalamus
PD	914	Posterodorsal preoptic nucleus	Hypothalamus
PS	1109	Parastrial nucleus	Hypothalamus
PVp	126	Periventricular hypothalamic nucleus, posterior part	Hypothalamus
PVpo	133	Periventricular hypothalamic nucleus, preoptic part	Hypothalamus
SBPV	347	Subparaventricular zone	Hypothalamus
SCH	286	Suprachiasmatic nucleus	Hypothalamus
SFO	338	Subfornical organ	Hypothalamus
VLPO	689	Ventrolateral preoptic nucleus	Hypothalamus
AHN	88	Anterior hypothalamic nucleus	Hypothalamus
LM	210	Lateral mammillary nucleus	Hypothalamus
MM	491	Medial mammillary nucleus	Hypothalamus
SUM	525	Supramammillary nucleus	Hypothalamus
TMd	1126	Tuberomammillary nucleus, dorsal part	Hypothalamus
TMv	1	Tuberomammillary nucleus, ventral part	Hypothalamus
MPN	515	Medial preoptic nucleus	Hypothalamus
PMd	980	Dorsal premammillary nucleus	Hypothalamus
PMv	1004	Ventral premammillary nucleus	Hypothalamus
PVhd	63	Paraventricular hypothalamic nucleus, descending division	Hypothalamus
VMH	693	Ventromedial hypothalamic nucleus	Hypothalamus
PH	946	Posterior hypothalamic nucleus	Hypothalamus
LHA	194	Lateral hypothalamic area	Hypothalamus
LPO	226	Lateral preoptic area	Hypothalamus
PST	356	Preparasubthalamic nucleus	Hypothalamus
PSTN	364	Parasubthalamic nucleus	Hypothalamus
RCH	173	Retrochiasmatic area	Hypothalamus
STN	470	Subthalamic nucleus	Hypothalamus
TU	614	Tuberal nucleus	Hypothalamus
ZI	797	Zona incerta	Hypothalamus
SCs	302	Superior colliculus, sensory related	Midbrain
IC	4	Inferior colliculus	Midbrain
NB	580	Nucleus of the brachium of the inferior colliculus	Midbrain
SAG	271	Nucleus sagulum	Midbrain
PBG	874	Parabigeminal nucleus	Midbrain
MEV	460	Midbrain trigeminal nucleus	Midbrain
SNr	381	Substantia nigra, reticular part	Midbrain
VTA	749	Ventral tegmental area	Midbrain
RR	246	Midbrain reticular nucleus, retrorubral area	Midbrain
MRN	128	Midbrain reticular nucleus	Midbrain
SCm	294	Superior colliculus, motor related	Midbrain
PAG	795	Periaqueductal gray	Midbrain
APN	215	Anterior pretectal nucleus	Midbrain
MPT	531	Medial pretectal area	Midbrain
NOT	628	Nucleus of the optic tract	Midbrain
NPC	634	Nucleus of the posterior commissure	Midbrain
OP	706	Olivary pretectal nucleus	Midbrain
PPT	1061	Posterior pretectal nucleus	Midbrain

Continued on next page

Continued from previous page

Abbreviation	Allen structure ID	Full structure name	Major brain division
CUN	616	Cuneiform nucleus	Midbrain
RN	214	Red nucleus	Midbrain
III	35	Oculomotor nucleus	Midbrain
IV	115	Trochlear nucleus	Midbrain
VTN	757	Ventral tegmental nucleus	Midbrain
AT	231	Anterior tegmental nucleus	Midbrain
LT	66	Lateral terminal nucleus of the accessory optic tract	Midbrain
SNC	374	Substantia nigra, compact part	Midbrain
PPN	1052	Pedunculopontine nucleus	Midbrain
IF	12	Interfascicular nucleus raphe	Midbrain
IPN	100	Interpeduncular nucleus	Midbrain
RL	197	Rostral linear nucleus raphe	Midbrain
CLI	591	Central linear nucleus raphe	Midbrain
DR	872	Dorsal nucleus raphe	Midbrain
NLL	612	Nucleus of the lateral lemniscus	Pons
PSV	7	Principal sensory nucleus of the trigeminal	Pons
PB	867	Parabrachial nucleus	Pons
SOC	398	Superior olfactory complex	Pons
B	280	Barrington's nucleus	Pons
DTN	880	Dorsal tegmental nucleus	Pons
PCG	898	Pontine central gray	Pons
PG	931	Pontine gray	Pons
PRNc	1093	Pontine reticular nucleus, caudal part	Pons
SG	318	Supragenual nucleus	Pons
SUT	534	Supratrigeminal nucleus	Pons
TRN	574	Tegmental reticular nucleus	Pons
V	621	Motor nucleus of trigeminal	Pons
CS	679	Superior central nucleus raphe	Pons
LC	147	Locus ceruleus	Pons
LDT	162	Laterodorsal tegmental nucleus	Pons
NI	604	Nucleus incertus	Pons
PRNr	146	Pontine reticular nucleus	Pons
RPO	238	Nucleus raphe pontis	Pons
SLC	350	Subceruleus nucleus	Pons
SLD	358	Sublaterodorsal nucleus	Pons
AP	207	Area postrema	Medulla
DCO	96	Dorsal cochlear nucleus	Medulla
VCO	101	Ventral cochlear nucleus	Medulla
CU	711	Cuneate nucleus	Medulla
GR	1039	Gracile nucleus	Medulla
ECU	903	External cuneate nucleus	Medulla
NTB	642	Nucleus of the trapezoid body	Medulla
NTS	651	Nucleus of the solitary tract	Medulla
SPVC	429	Spinal nucleus of the trigeminal, caudal part	Medulla
SPVI	437	Spinal nucleus of the trigeminal, interpolar part	Medulla
SPVO	445	Spinal nucleus of the trigeminal, oral part	Medulla
VI	653	Abducens nucleus	Medulla
VII	661	Facial motor nucleus	Medulla
ACVII	576	Accessory facial motor nucleus	Medulla
AMB	135	Nucleus ambiguus	Medulla
DMX	839	Dorsal motor nucleus of the vagus nerve	Medulla
GRN	1048	Gigantocellular reticular nucleus	Medulla
ICB	372	Infracerebellar nucleus	Medulla
IO	83	Inferior olfactory complex	Medulla
IRN	136	Intermediate reticular nucleus	Medulla
ISN	106	Inferior salivatory nucleus	Medulla
LIN	203	Linear nucleus of the medulla	Medulla
LRN	235	Lateral reticular nucleus	Medulla
MARN	307	Magnocellular reticular nucleus	Medulla
MDRNd	1098	Medullary reticular nucleus, dorsal part	Medulla
MDRNv	1107	Medullary reticular nucleus, ventral part	Medulla
PARN	852	Parvicellular reticular nucleus	Medulla
PAS	859	Parasolitary nucleus	Medulla
PGRNd	970	Paragigantocellular reticular nucleus, dorsal part	Medulla
PGRNI	978	Paragigantocellular reticular nucleus, lateral part	Medulla

Continued on next page

Continued from previous page

Abbreviation	Allen structure ID	Full structure name	Major brain division
NR	177	Nucleus of Roller	Medulla
PRP	169	Nucleus prepositus	Medulla
PPY	1069	Parapyramidal nucleus	Medulla
LAV	209	Lateral vestibular nucleus	Medulla
MV	202	Medial vestibular nucleus	Medulla
SPIV	225	Spinal vestibular nucleus	Medulla
SUV	217	Superior vestibular nucleus	Medulla
x	765	Nucleus x	Medulla
XII	773	Hypoglossal nucleus	Medulla
y	781	Nucleus y	Medulla
LING	912	Lingula (I)	Cerebellum
CENT	920	Central lobule	Cerebellum
CUL	928	Culmen	Cerebellum
DEC	936	Declive (VI)	Cerebellum
FOTU	944	Folium-tuber vermis (VII)	Cerebellum
PYR	951	Pyramus (VIII)	Cerebellum
UVU	957	Uvula (IX)	Cerebellum
NOD	968	Nodulus (X)	Cerebellum
SIM	1007	Simple lobule	Cerebellum
AN	1017	Ansiform lobule	Cerebellum
PRM	1025	Paramedian lobule	Cerebellum
COPY	1033	Copula pyramidis	Cerebellum
PFL	1041	Paraflocculus	Cerebellum
FL	1049	Flocculus	Cerebellum
FN	989	Fastigial nucleus	Cerebellum
IP	91	Interposed nucleus	Cerebellum
DN	846	Dentate nucleus	Cerebellum